

Drop rebound at low Weber number

Chase T. Gabbard^{1,†}, Elvis A. Agüero¹, Radu Cimpanu², Katharina Kuehr³, Eli Silver¹, Jack-William Barotta¹, Carlos A. Galeano-Rios³,
and Daniel M. Harris^{1,‡}

¹School of Engineering, Brown University, Providence, RI 02912, USA

²Mathematics Institute, University of Warwick, Coventry CV4 7AL, UK

³College of Computational Sciences, Minerva University, San Francisco, CA 94103, USA

(Received xx; revised xx; accepted xx)

We study the rebound of drops impacting non-wetting substrates at low Weber number We through experiment, direct numerical simulation, and reduced-order modeling. Submillimeter-sized drops are normally impacted onto glass slides coated with a thin viscous film that allows them to rebound without contact line formation. Experiments are performed with various drop viscosities, sizes, and impact velocities, and we directly measure metrics pertinent to spreading, retraction, and rebound using high-speed imaging. We complement experiments with direct numerical simulation and a fully predictive reduced-order model that applies natural geometric and kinematic constraints to simulate the drop shape and dynamics using a spectral method. At low We , drop rebound is characterized by a weaker dependence of the coefficient of restitution on We than in the more commonly studied high- We regime, with nearly We -independent rebound in the inertio-capillary limit, and an increasing contact time as We decreases. Drops with higher viscosity or size interact with the substrate longer, have a lower coefficient of restitution, and stop bouncing sooner, in good quantitative agreement with our reduced-order model. In the inertio-capillary limit, low We rebound has nearly symmetric spreading and retraction phases and a coefficient of restitution near unity. Increasing We or viscosity breaks this symmetry, coinciding with a drop in the coefficient of restitution and an increased dependence on We . Lastly, the maximum drop deformation and spreading are related through energy arguments, providing a comprehensive framework for drop impact and rebound at low We .

Key words: drops, capillary flows

1. Introduction

Drop impacts are common in everyday life, industry, and nature. Examples include drops splashing on a kitchen sink, precision inkjet printing (Lohse 2022), and raindrops striking leaves and animal fur (Roth-Nebelsick *et al.* 2022). Since the seminal studies of Worthington (Worthington 1877, 1908) and Edgerton’s iconic images (Edgerton & Killian 1954), researchers have strived to uncover the physics of impact phenomena, which include drop deposition, splashing, and rebound (Rein 1993; Yarin 2006). Early studies primarily focused on splashing, but interest in drop rebound has surged, inspired in part by raindrops bouncing off superhydrophobic leaves (Chen *et al.*

† Email address for correspondence: chase_gabbard@brown.edu

‡ Email address for correspondence: daniel_harris3@brown.edu

2011) and driven by advances in surface preparation techniques that can render surfaces hydrophobic and enable rebound (Richard & Qu  r   2000; Okumura *et al.* 2003). Despite the impact of these innovations on numerous everyday items, such as windshields and eyewear, our understanding of the physics governing rebound is mostly limited to millimeter-sized drops striking surfaces at moderate and high speeds. This paucity motivates a detailed study of low speed rebound of submillimetric drops, which are typical in commercial spray nozzles (Makhnenko *et al.* 2021; Chen & Ashgriz 2022), naturally emerge from ligament breakup (Villermaux 2020), and can result from splashing of millimetric drops (Yarin 2006). Recent attempts to fill this knowledge gap have been afflicted with contact line friction, which increasingly alters the rebound physics as the impact velocity decreases (Wang *et al.* 2022; Thenarianto *et al.* 2023). To address this knowledge gap, we perform experiments on a perfectly non-wetting substrate—a thin viscous film—using submillimeter-sized drops and identify the relevant physics governing rebound using reduced-order modeling, direct numerical simulation, and energetic arguments.

Over a century ago, Lord Rayleigh observed drops rebounding upon impact (Rayleigh 1879) and attributed this phenomenon to an intervening air layer separating the drops and preventing coalescence (Rayleigh 1899). Since then, experiments conducted under modified atmospheric conditions and corresponding theoretical studies have confirmed his hypothesis (Willis & Orme 2000; Bach *et al.* 2004; Chubynsky *et al.* 2020). Meanwhile, advancements in experimental and computational techniques have enabled measurement of the minimum thickness of the air layer—on the order of 100 nm—below which van der Waals forces bridge the liquid-air interfaces and capillary forces drive coalescence (Couder *et al.* 2005a; de Ruiter *et al.* 2012; Kolinski *et al.* 2012; Kavehpour 2015; Sprittles 2024; Lewin-Jones *et al.* 2024). Thus, drops only rebound without contact from smooth surfaces. Although there are limited solid surfaces smooth enough to promote contactless rebound, liquid-gas interfaces are atomically smooth and ideal for rebound. For example, recent results for the rebound of a drop on a bath of the same fluid showed that the deformation of the drop and bath are dynamically coupled (Alventosa *et al.* 2023; Phillips & Milewski 2024), and that vibrating the bath can lead to long-lasting bouncing and wave-propelled drop motion (Couder *et al.* 2005b; Mol    ek & Bush 2013). This dynamic coupling is further evidenced by the complex bubble patterns observed when an impacting drop merges with a bath (Saylor & Bounds 2012). If the bath height is reduced to a thin film, rebound can become substrate-independent (Hao *et al.* 2015; Sanjay *et al.* 2023b). Although drops can rebound from heated substrates (Biance *et al.* 2006), dry ice (Li *et al.* 2024), and when the drop is coated with hydrophobic powder (Aussillous & Qu  r   2006), these methods inject energy into the system or modify the drop composition, potentially altering the rebound dynamics and obfuscating the fundamental physics.

Rebound dynamics are governed by a competition of inertial, viscous, capillary, and gravitational forces. A common set of governing dimensionless parameters describing the problem are

$$We = \frac{\rho V^2 R}{\sigma}, \quad Bo = \frac{\rho g R^2}{\sigma}, \quad Oh = \frac{\mu}{\sqrt{\rho \sigma R}}. \quad (1.1)$$

The Weber number We compares inertial and surface tension forces, Bond number Bo compares gravitational and surface tension forces, and Ohnesorge number Oh is the ratio of the inertio-capillary to the viscous timescale. Here, R is the undeformed drop radius, V is the impact velocity, ρ is the liquid density, μ is the dynamic viscosity, σ is the surface tension coefficient, and g is the gravitational acceleration. Although early studies emphasized We as the primary parameter controlling rebound (Foote 1975;



Figure 1: A drop of silicone oil ($R = 0.31$ mm) rebounding from a glass slide coated with a thin, viscous film ($\Gamma/Oh_f^{1/3} \approx 10^{-2}$). Here, $We = 1.03$, $Oh = 0.02$, and $Bo = 0.04$. Subsequent images are separated by 1.44 ms and shifted 0.4 mm to the right.

Anders *et al.* 1993; Richard & Quéré 2000; Richard *et al.* 2002; Okumura *et al.* 2003), recent work has shown that increasing Bo and Oh can suppress rebound for $We > 1$ (Jha *et al.* 2020; Sanjay *et al.* 2023a). For $We < 1$, the role of Bo and Oh is less explored, and attempts to isolate the role of We on rebound have been confounded by the increasing influence of contact line friction as We decreases (Wang *et al.* 2022; Thenarianto *et al.* 2023). Impacting a drop on a substrate coated with a viscous film avoids contact line formation, as discussed by Gilet *et al.* (2008) and Gilet & Bush (2012). This technique produces substrate-independent rebound when the film is sufficiently thin and viscous (Hao *et al.* 2015). To determine the criteria where drop rebound is substrate-independent, Sanjay *et al.* (2023b) analyzed the competing influences of the drop Ohnesorge number Oh and film Ohnesorge number $Oh_f = \mu_f / (\rho \sigma R)^{1/2}$, and found that substrate-independent rebound occurs for $Oh_f \gtrsim 0.1$ when $\Gamma < B Oh_f^{1/3}$, where $\Gamma = h_f/R$ and $B = B(Oh)$. Since $B \approx 0.1$ when $Oh \approx 0.1$, and B increases with decreasing Oh , a conservative condition for substrate-independent bouncing is $\Gamma/Oh_f^{1/3} < 0.1$. Notably, this result is derived for $We > 1$ and becomes less restrictive for $We < 1$. By following these guidelines, a rigid substrate can be prepared that allows a drop to rebound without contact line formation or dynamic influence from the viscous film. An example of such a rebound is imaged in figure 1.

When a drop impacts a rigid substrate, it first spreads until reaching a maximum equatorial radius R_m and maximum contact radius R_c . When $We \gg 1$, the dimensionless maximum equatorial radius $\beta = R_m/R$ and maximum contact radius $\beta_c = R_c/R$ are approximately equal, and two competing scaling laws have been proposed to describe their evolution with We . Clanet *et al.* (2004) proposed $\beta \sim We^{1/4}$ based on momentum conservation and assuming the drop deforms into a cylinder with negligible height during impact. Alternatively, the conservation of energy between the kinetic energy of the drop at impact and the surface energy at the maximum deformation of the drop predicts $\beta \sim We^{1/2}$ (Chandra & Avedisian 1991; Bennett & Poulikakos 1993;

Okumura *et al.* 2003). Although additional arguments and empirical evidence favor the scaling $We^{1/2}$ (Eggers *et al.* 2010; Villiermaux & Bossa 2011; Laan *et al.* 2014; Lee *et al.* 2016; Josserand & Thoroddsen 2016), extensive experimental results support the scaling $We^{1/4}$ over a wide range of We (Bartolo *et al.* 2005; Biance *et al.* 2006; Tsai *et al.* 2011; García-Geijo *et al.* 2020; Zhan *et al.* 2021; Li *et al.* 2024). When viscous forces are important, these scalings break down (Rein 1993), and describing the crossover from the capillary to viscous regime requires consideration of finite Oh effects (or $Re = \sqrt{We}/Oh = \rho VR/\mu$) (Roisman 2009; Eggers *et al.* 2010; Laan *et al.* 2014; Lee *et al.* 2016; Sanjay & Lohse 2025). For $We < 1$, the deformed drop resembles an oblate ellipsoid rather than a wide cylinder and $\beta \not\approx \beta_c$. In this case, Richard & Qu     (2000) predicted $\beta - 1 = (5/48)^{1/2} We^{1/2}$ by assuming the initial kinetic energy of the drop was converted to surface energy but did not test their prediction across a range of We . Recently, efforts to describe and relate β and β_c during low We rebound have used drops with non-negligible Bo and relied on fits to empirical relations (Liu *et al.* 2023; Li *et al.* 2024). Thus, a comprehensive and validated understanding of spreading for low We is still lacking.

Following spreading, surface tension drives the drop to retract and can lead to rebound. When Oh is negligible, the maximum retraction rate is independent of impact velocity, and the retraction time $t_r \sim t_\sigma$, where $t_\sigma = (\rho R^3/\sigma)^{1/2}$ is the intertio-capillary time (Bartolo *et al.* 2005). This result is valid for $We > 1$, and since inertia also governs the spreading time t_s , the interaction time between the substrate and drop $t_c = t_s + t_r$, referred to as the contact time henceforth, scales as $t_c \sim A t_\sigma$ (Richard *et al.* 2002), where $A = f(Oh)$ (Jha *et al.* 2020). Alternatively, when $We < 1$, the non-dimensional contact time t_c/t_σ increases as We decreases (Foote 1975; Okumura *et al.* 2003). This transition in We dependence signals a shift in the underlying physics. This shift also alters the We dependence of the coefficient of restitution ε , a measure of the elasticity of the rebound. For $We > 1$, Anders *et al.* (1993) noted that ε is We dependent and Biance *et al.* (2006) showed that $\varepsilon \sim We^{-1/2}$, which has been verified on various rigid substrates (Wang *et al.* 2022; Thenarianto *et al.* 2023). Additionally, Jha *et al.* (2020) showed that increasing Oh decreases the coefficient of restitution ε . For $We < 1$, Gilet & Bush (2012) suggested We -independent rebound such that $\varepsilon = f(Oh)$. Recent efforts to study ε for low We rebounds observed a peak in ε as We decreases, followed by a decrease to $\varepsilon = 0$ (no rebound) at finite We (Wang *et al.* 2022; Thenarianto *et al.* 2023). The suggested functional form of this decrease $\varepsilon \sim We^{1/2}$ is attributed to contact line friction, highlighting the need for contact line-free conditions to determine the ε - We relationship at low We .

These unique trends in the rebound metrics at low We have inspired several models. Okumura *et al.* (2003) derived a simple model for the contact time t_c and maximum equatorial deformation β by treating the drop as a spring-mass system, with spring constant scaling with the surface tension coefficient. Jha *et al.* (2020) expanded this model to include damping to describe the rebound dynamics of viscous drops. Mol       & Bush (2012) proposed a quasi-static model for impacts on non-wetting surfaces, approximating drop shapes as static during impact, giving analytical predictions for t_c and ε in various limits. Concurrently, Chevy *et al.* (2012) derived a quasi-static model for the droplet deformation, highlighting the non-linear elastic behavior of weakly deformed drops. More recently, Galeano-Rios *et al.* (2017) introduced a kinematic match (KM) method to derive a fully predictive model for the rebound of a rigid hydrophobic sphere on a liquid bath, which has been extensively validated through experiments and direct numerical simulation (Galeano-Rios *et al.* 2017, 2019, 2021). The KM method imposes natural kinematic and geometric constraints on the motion of interacting surfaces, ensuring

continuity at the contact interface. This approach is particularly well-suited for rebound problems as it provides a robust framework to capture the interplay between fluid dynamics and interfaces, making it highly versatile for a wide range of impact scenarios in mechanics. For example, Agüero *et al.* (2022) applied the KM method to non-Hertzian impact of a solid sphere on an elastic membrane and observed good agreement with experiment. These successful applications of the KM method and its ability to efficiently simulate rebound phenomena with minimal assumptions motivate its extension to drop rebound on rigid substrates.

Herein, we present experiments and direct numerical simulation results of drop rebound at low We , and develop a robust reduced-order model using the KM method. The experimental apparatus, testing protocol, and image processing technique are detailed in § 2. In § 3 we present the formulation of our reduced-order model and describe our direct numerical simulation (DNS) framework. In § 4, we compare our experiments and DNS results with our model predictions for the pertinent metrics describing drop rebound (§ 4.1), spreading and retraction dynamics (§ 4.2), and maximum drop deformation and spreading (§ 4.3). In § 5 we synthesize our findings into new knowledge about drop rebound and contextualize it within the existing literature. Finally, we summarize our key findings in § 6 and identify a number of open questions inspired by this work.

2. Experiment

2.1. Experimental setup

We performed experiments using a 3D-printed drop generator mounted on a motorized linear stage to produce submillimeter-sized silicone oil drops with less than 1% variability (Harris *et al.* 2015; Ionkin & Harris 2018), as illustrated in figure 2(a). The latest design, employed for this work, is documented at <https://github.com/harrislab-brown/DropGen>. Among other improvements, this design allows for precise height control via a motorized linear stage and is adapted to use commercially available nozzles from Fused Deposition Modeling (FDM) 3D-printers. The drop generator expels a thin liquid jet from a nozzle by deforming a piezoelectric disk and then quickly relaxes it, retracting the thin jet while surface tension drives pinch-off a single drop. By timing drop pinch-off to occur as the jet retracts, the drop is directed upward and ‘floats’ momentarily, allowing interfacial oscillations to decay considerably. Here, we report only experiments where the ratio of the drops diameter in the horizontal and vertical directions is between 0.96 and 1.04 just before impact to minimize the effect of residual drop oscillations on the rebound metrics (Biance *et al.* 2006; Yun & Kim 2019). Supplemental movie 1 demonstrates drop generation. The radius of the drop R and its velocity at impact V were varied by using nozzles with different inner diameters and changing the distance between the nozzle and substrate, respectively. The working fluids were silicone oils (Clearco Products) with slightly varying density ρ and surface tension σ , but a wide range of dynamic viscosity μ , which allowed us to explore the role of drop viscosity on rebound. The ranges of the dimensional and non-dimensional parameters explored are summarized in table 1.

An atomically smooth, non-wetting substrate was prepared by coating a standard glass slide with a thin film of viscous silicone oil (Gilet & Bush 2012; Hao *et al.* 2015; Sanjay *et al.* 2023b). To achieve this, we first coated the slide with a thick layer of viscous silicone oil $\mu = 975 \text{ g cm}^{-1}\text{s}^{-1}$. Then, the slide was passed beneath a fixed knife edge to thin and level the film. The mean film thickness h_f was measured by weighing the slide, and was $h_f = 231 \pm 55 \text{ }\mu\text{m}$ across all experiments. This thickness corresponds to a dimensionless film thickness $\Gamma = h_f/R \approx 10^0$ and film mobility $\Gamma/Oh_f^{1/3} \approx 10^{-2}$

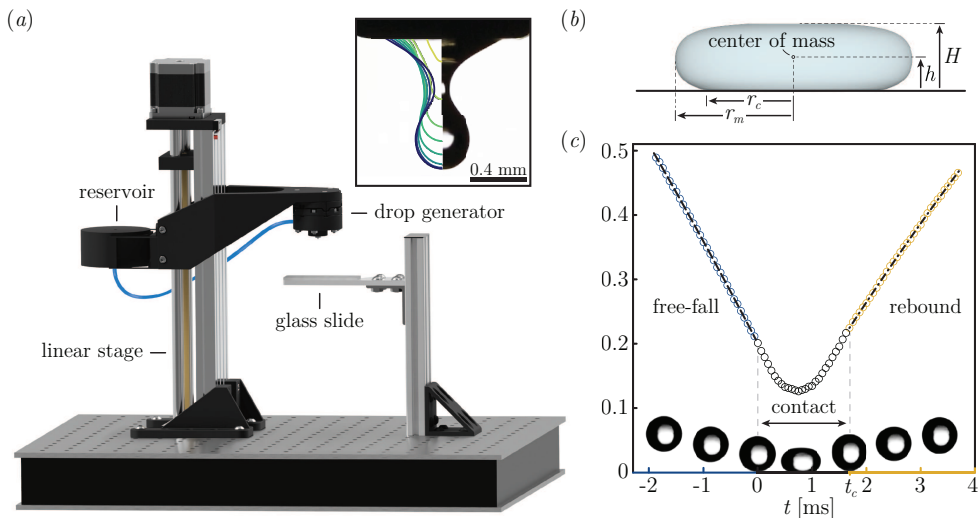


Figure 2: (a) A rendering of the experimental setup. The inset depicts the drop generation process with the evolution of the liquid-air interface (left half) illustrated with colored lines increasing with time from yellow (light) to blue (dark). (b) Schematic of an impacting drop and measured variables. (c) Height of the center of mass h against time t for a rebounding drop ($R = 0.2$ mm), where $We = 0.25$, $Oh = 0.03$, and $Bo = 0.02$. Dashed and dot-dashed lines are parabolic fits to the drop position during free-fall and rebound, respectively. Gray dashed lines indicate the initial contact time $t = 0$ and detachment time $t = t_c$.

Parameter	Symbol	Units (cgs)	Range
Drop radius	R	cm	0.0094 – 0.0967
Impact velocity	V	cm s^{-1}	1.00 – 74.39
Density	ρ	g cm^{-3}	0.850 – 0.975
Surface tension	σ	g s^{-2}	18.7 – 20.8
Dynamic viscosity	μ	$\text{g cm}^{-1} \text{s}^{-1}$	0.0187 – 0.4785
Gravitational acceleration	g	cm s^{-2}	981
Weber number	We	—	0.0008 – 10.6185
Ohnesorge number	Oh	—	0.0139 – 0.7865
Bond number	Bo	—	0.0037 – 0.4197

Table 1: Parameter ranges explored in our experiments.

that is well below the $\Gamma/Oh_f^{1/3} \leq 10^{-1}$ criterion discussed earlier and thus confidently within the regime of substrate-independent drop bouncing (Sanjay *et al.* 2023b). After the slide was prepared it was placed in a closed environment for at least 12 hours to allow non-uniformities in the film to relax under gravity. During testing, the substrate was mounted perpendicular to the direction of gravitational acceleration to ensure the air layer between the impacting drop and substrate did not rupture prematurely due to asymmetry (Lo *et al.* 2017).

2.2. Experimental protocol

To begin a set of experiments, a reservoir connected to the drop generator is filled with silicone oil, and the system is manually purged to remove any trapped air (Harris *et al.* 2015). Next, the pulse width controlling the piezoelectric disks actuation is tuned to produce a single drop with minimal surface oscillations at impact. These settings vary based on the working fluid and nozzle. Next, the nozzle is lowered until it rests just above the substrate, and the system height is set to zero. The nozzle is raised to the desired initial drop height, typically 1 or 2 mm, and a droplet is generated. The drop falls under the action of gravity and its motion is recorded from release until bouncing ceases. After coming to rest, an external pulse of air is applied and sweeps the drop from the substrate before it can coalesce with the film, ensuring the surface remains pristine for subsequent experiments. In the few cases where the drop merged with the viscous film, the slide was translated so the next impact occurred sufficiently far from the merge site. The nozzle height is raised incrementally, and three to eight drops are recorded at each height. The experiments conclude once impact stresses become strong enough to pierce the intervening air layer (Hao *et al.* 2015), which occurs at $We \approx 10$ for all Oh , or drop retraction leads to droplet ejection for low Oh drops (Richard & Qu  r   2000; Bartolo *et al.* 2006), as shown in supplemental movie 2.

The silhouette of the drop was illuminated by an LED backlight and recorded using a Phantom Miro LC311 high-speed camera with a Laowa 25 mm ultra-macro lens. The frame rate ranged from 9,000 to 20,000 fps. The pixel size in the recordings was calibrated using a microscope calibration slide. The spatial resolution in our experiments varied between 0.003 and 0.008 mm depending on the size of the drop—smaller drops required higher magnification—but, in general, was approximately $0.02R$. Recordings of each experiment were processed using MATLAB to identify the drop silhouette using Canny edge detection and calculated its center of mass by assuming the drop shape is a surface of revolution about the vertical axis passing through its centroid, and the drop has uniform density. Time was defined such that $t = 0$ when the drop “contacts” the substrate and $t = t_c$ when it detaches, where the drop and substrate are considered in “contact” when a portion of the drop and substrate occupy the same pixel. As noted previously, no actual contact occurs between the droplet and substrate due to the microscopic mediating air layer. During rebound, the vertical location of the center of mass h and top of the drop H are tracked, as well as the equatorial radius r_m and contact radius r_c of the drop, as defined in figure 2(b). We define H as the maximum vertical distance between the substrate and any point on the surface of the drop. Consequently, when drop deformation is small, the region at the north pole of the drop is convex upward and H coincides with the drop height along the vertical axis passing through its centroid. When drop deformation is large, the location along the surface of the drop where H is measured shifts toward its rim.

We calculate the undisturbed drop radius R by measuring the average projected area of the drop in the 30 frames preceding impact, and then solve for R assuming the projected area is a circle. The center of mass h during these frames is fit to a parabola and the velocity of the drop at impact is $V = dh/dt(t = 0)$. Similarly, the rebound velocity is $V_r = dh/dt(t = t_c)$, where h is fit to a parabola for the 30 frames following detachment. For experiments where less than 30 frames separated detachment and subsequent impact, all intervening frames were used to calculate V_r . Figure 2(c) plots the center of mass of a drop h against time t , before (blue markers), during (black markers), and after impact (yellow markers) for $We = 0.25$, $Oh = 0.03$, and $Bo = 0.02$. The vertical dashed lines indicate the initial contact time $t = 0$ and detachment time $t = t_c$ of the drop, and the

dashed and dot-dashed black curves are parabolic fits for h during free-fall and rebound, respectively. Snapshots of the drop shape during free-fall, contact, and rebound are inset.

The elasticity of rebound can be characterized by the coefficient of restitution ε

$$\varepsilon^2 = \frac{E_r}{E_i} = \frac{g(h(t_c) - R) + 0.5V_r^2}{0.5V^2}, \quad (2.1)$$

which compares the energy of the drop at rebound E_r and impact E_i . Although E_i is purely kinetic, E_r has kinetic and gravitational potential contributions owing to drop deformation at detachment. In most prior studies the potential energy has been ignored and $\varepsilon = V_r/V$ (Richard & Qu  r   2000; Biance *et al.* 2006; De Ruiter *et al.* 2015; Hao *et al.* 2015; Jha *et al.* 2020). Ignoring potential energy implies a spherical drop at detachment (Richard & Qu  r   2000), and is not always negligible when the kinetic energy is small for $We < 1$. A drop can be elongated at detachment when $We < 1$, as shown in the images inset in figure 2(c). Other authors defined E_r as the gravitational potential energy of the drop at its maximum height after rebound, but this definition ignores possible viscous loss due to the surrounding air during free flight (Wang *et al.* 2022; Thenariento *et al.* 2023). Our definition does not make any of these assumptions, providing energetically consistent and accurate measurements at low We .

The uncertainty of each measurement was determined by considering the spatial and temporal resolution of our experimental setup. The temporal resolution is related to the time between successive frames $\Delta t = 0.5 \text{ (fps)}^{-1}$ and the spatial resolution is calculated using the width of a pixel L_p , as $\Delta L = 0.5 (L_p)^{-1}$. To estimate the uncertainty in the velocity, we first calculated the residuals between the measured center of mass height h and the fitted parabola. The standard deviation of these residuals σ_{res} served as a measure of the uncertainty in the position data. This uncertainty is propagated to the velocity estimate by assuming that the uncertainty in the velocity is equal to the standard deviation of the residuals, scaled by the curvature of the fitted parabola, $\delta V \approx 0.5 \sigma_{\text{res}} |2a|$, where a is the quadratic coefficient of the fitted parabola. Uncertainty propagation was performed using Mathematica, where first-order Taylor expansion was used for uncertainty propagation and uncertainties were assumed uncorrelated.

3. Modeling and simulations

3.1. Kinematic match model formulation

We consider a drop of incompressible fluid of constant density ρ , dynamic viscosity μ , and surface tension coefficient σ impacting normally on a perfectly hydrophobic (non-wetting), horizontal solid substrate. Before impact, the droplet is spherical with radius R and the surface of the droplet is stationary relative to its center of mass. During impact the drop is “pressed” to the substrate rather than in true physical “contact” with it; however, we will use the later in our discussion for consistency and connection with the prior literature. The criteria for contact and its implication on the model results are discussed in Appendix A.

We introduce spherical coordinates (ζ', θ, ϕ) with $\theta \in [0, \pi]$ and $\phi \in [0, 2\pi]$ (where $'$ indicates a dimensional variable) to describe the free surface of the drop. Here, θ is measured relative to the direction of gravity, and the origin is at the center of mass of the drop. Due to the assumed axisymmetry, the azimuthal angle ϕ can be ignored, consistent with experiments for all cases considered here. Additionally, we define the associated Cartesian system of coordinates (x', z') , as shown in figure 3(a) for an impacting drop. This formulation allows the smooth drop shape to be discretized, as shown in figure 3(b),

and permits numerical approximations that enable efficient simulation of drop rebound across a wide range of We .

3.1.1. Drop motion

The drop is subject to gravitational acceleration $g\hat{\mathbf{z}}$, and the substrate is at a distance h' from its center of mass. At time $t' = 0$, $h' = R$, and the center of mass of the drop moves towards the substrate with velocity V . The fluid motion within the drop is governed by the Navier-Stokes equations for incompressible flow, with standard kinematic and dynamic boundary conditions. The normal impact on the substrate is modeled by an evolving pressure distribution over the contact area $S(t)$, where the drop surface and substrate coincide in the model.

Following Alventosa *et al.* (2023), we linearize the governing equations and represent the surface deformation of the drop η' as a sum of axisymmetric spherical harmonic modes:

$$\eta' := \zeta' - R = \sum_{l=2}^{\infty} \mathcal{A}'_l P_l(\cos(\theta)). \quad (3.1)$$

Here, P_l are Legendre polynomials, and \mathcal{A}'_l denotes the time-dependent amplitude of the l^{th} mode. The $l = 0$ mode is excluded due to incompressibility. The $l = 1$ mode is also excluded in the present formulation due to the choice of the drop's center of mass as the origin, since the $l = 1$ mode shifts the center of mass. Figure 3(c) demonstrates the synthesis of Legendre polynomials for modes $l = 2 - 4$ into a sample deformed drop shape. Similarly, the contact pressure p' exerted by the substrate on the drop is expressed as

$$p' = \sum_{l=0}^{\infty} \mathcal{B}'_l P_l(\cos(\theta)), \quad (3.2)$$

where \mathcal{B}'_l is the time-dependent amplitude of the l^{th} Legendre mode.

The evolution of the drop interface is obtained by applying linearized kinematic conditions on the surface in the weakly damped and small-amplitude regime (Lamb 1924; Miller & Scriven 1968; Phillips & Milewski 2024)

$$\mathcal{A}'_l = \mathcal{U}'_l, \quad \text{for } l = 2, 3, \dots, \infty; \quad (3.3)$$

$$\dot{\mathcal{U}}'_l = -\frac{\sigma l(l+2)(l-1)}{\rho R^3} \mathcal{A}'_l - 2(2l+1)(l-1) \frac{\mu}{\rho R^2} \mathcal{U}'_l - \frac{l}{\rho R} \mathcal{B}'_l, \quad \text{for } l = 2, \dots, \infty, \quad (3.4)$$

where \mathcal{U}'_l is the amplitude of the l^{th} Legendre mode of the surface's velocity, $\dot{\zeta}'$. Equations (3.3) and (3.4) are subject to

$$\mathcal{A}'_l(t=0) = 0, \quad \text{for } l = 2, \dots, \infty; \quad (3.5)$$

$$\mathcal{U}'_l(t=0) = 0, \quad \text{for } l = 2, \dots, \infty. \quad (3.6)$$

The height of the center of mass is naturally governed by Newton's second law of motion,

$$\dot{h}' = v', \quad (3.7)$$

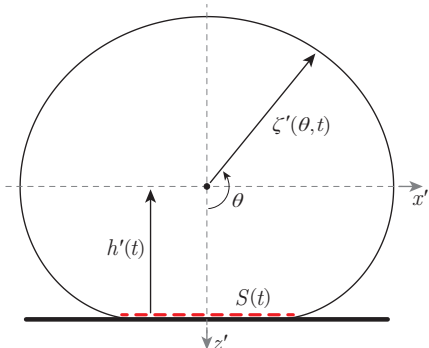
$$\dot{v}' = -g + \frac{1}{m} \frac{4\pi R^2}{3} \mathcal{B}'_1, \quad (3.8)$$

subject to

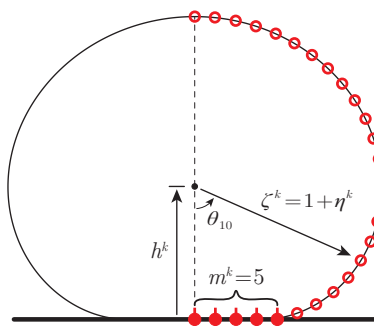
$$h'(t=0) = R, \quad (3.9)$$

$$v'(t=0) = -V, \quad (3.10)$$

(a)



(b)



(c)

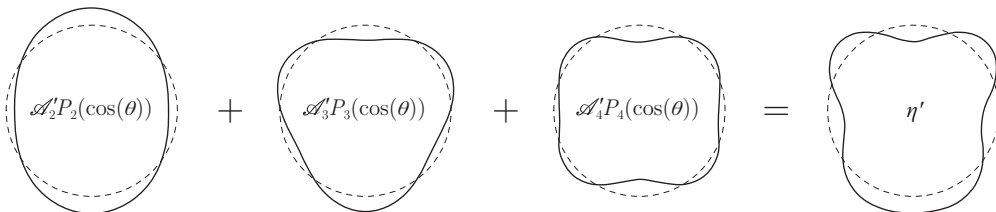


Figure 3: (a) Schematic of an axisymmetric drop impacting a rigid substrate, where $\zeta'(\theta, t)$ is the dimensional interface, $h'(t)$ the height of the center of mass of the drop, and $S(t)$ the contact surface. (b) Angular discretization of the right hemisphere of an axisymmetric drop during impact. Filled circles represent mesh points where the drop and substrate touch, while hollow circles denote points along the liquid-gas interface. (c) An example of shape reconstruction through Legendre synthesis for modes $l = 2 - 4$.

where $m = \frac{4\pi}{3}\rho R^3$ is the mass of the drop and g is gravitational acceleration.

3.1.2. The kinematic match

The motion of the drop's surface must satisfy additional compatibility conditions. Namely, when the substrate exerts pressure on the drop, a circular contact area $\theta \leq \theta_c$ forms, which must lie on the $z' = 0$ plane. That is

$$\sum_{l=2}^{\infty} \mathcal{A}'_l P_l(\cos(\theta)) = \frac{h'}{\cos(\theta)} - R, \quad \text{for } \theta \leq \theta_c. \quad (3.11)$$

Outside the contact area, the drop surface must be strictly above the solid surface,

$$\sum_{l=2}^{\infty} \mathcal{A}'_l P_l(\cos(\theta)) > \frac{h'}{\cos(\theta)} - R, \quad \text{for } \theta > \theta_c, \quad (3.12)$$

and the contact pressure there must be null, that is,

$$\sum_{l=0}^{\infty} \mathcal{B}'_l P_l(\cos(\theta)) = 0, \quad \text{for } \theta > \theta_c. \quad (3.13)$$

Finally, at the boundary of the contact area, the drop surface must be tangent to the substrate,

$$\frac{\partial}{\partial \theta} \left[\left(R + \sum_{l=2}^{\infty} \mathcal{A}'_l P_l(\cos(\theta)) \right) \cos(\theta) \right]_{\theta=\theta_c} = 0, \quad (3.14)$$

which captures the non-wetting nature of the surface. Our formulation results in a fully self-contained model without fitting parameters, which we can now non-dimensionalize.

3.1.3. Non-dimensionalization

The characteristic length, mass, and time are taken to be the undeformed droplet radius R , mass scale ρR^3 , and the inertio-capillary time $t_\sigma = ((\rho R^3)/\sigma)^{1/2}$, respectively. We also define the Bond number Bo , Weber number We , and Ohnesorge number Oh as in equation (1.1). This process leads to the dimensionless equations:

$$\dot{\mathcal{A}}_l = \mathcal{U}_l, \quad \text{for } l = 2, \dots, \infty; \quad (3.15)$$

$$\dot{\mathcal{U}}_l = -l(l+2)(l-1)\mathcal{A}_l - 2(2l+1)(l-1)Oh \mathcal{U}_l - l\mathcal{B}_l, \quad \text{for } l = 2, \dots, \infty; \quad (3.16)$$

$$\dot{h} = v; \quad (3.17)$$

$$\dot{v} = -Bo + \mathcal{B}_1; \quad (3.18)$$

which are subject to

$$\mathcal{A}_l(t=0) = 0, \quad \text{for } l = 2, \dots, \infty; \quad (3.19)$$

$$\mathcal{U}_l(t=0) = 0, \quad \text{for } l = 2, \dots, \infty; \quad (3.20)$$

$$h(t=0) = 1; \quad (3.21)$$

$$v(t=0) = -\sqrt{We}; \quad (3.22)$$

$$\sum_{l=2}^{\infty} \mathcal{A}_l P_l(\cos(\theta)) = \frac{h}{\cos(\theta)} - 1, \quad \text{for } \theta \leq \theta_c; \quad (3.23)$$

$$\sum_{l=2}^{\infty} \mathcal{A}_l P_l(\cos(\theta)) > \frac{h}{\cos(\theta)} - 1, \quad \text{for } \theta > \theta_c; \quad (3.24)$$

$$\sum_{l=0}^{\infty} \mathcal{B}_l P_l(\cos(\theta)) = 0, \quad \text{for } \theta > \theta_c; \quad (3.25)$$

$$\frac{\partial}{\partial \theta} \left[\left(1 + \sum_{l=2}^{\infty} \mathcal{A}_l P_l(\cos(\theta)) \right) \cos(\theta) \right]_{\theta=\theta_c} = 0. \quad (3.26)$$

We solve this system of equations by first applying numerical approximations, detailed in appendix B. Briefly, these include truncating the expansions of the surface shape, velocity, and pressure distribution with a spectral mesh consisting of Legendre polynomials up to degree $L = 90$ and approximating time derivatives using a first-order implicit Euler method. All simulations used to generate the results in the remaining figures of this paper adopt this value of L . A schematic of the angular mesh is shown in figure 3(b). The result of these approximations is a discrete optimization problem, which we solve using an adaptive timestep and error minimization scheme, as described in appendix C. This approach accurately solves the system at reduced computation cost relative to DNS, with the longest simulations completing in $\mathcal{O}(10)$ CPU minutes and a typical simulation time of less than 1 CPU minute.

3.2. Direct numerical simulation

We develop a computational framework based on the Basilisk open-source code structure (Popinet 2009, 2015) as a comparative benchmark for the mathematical model

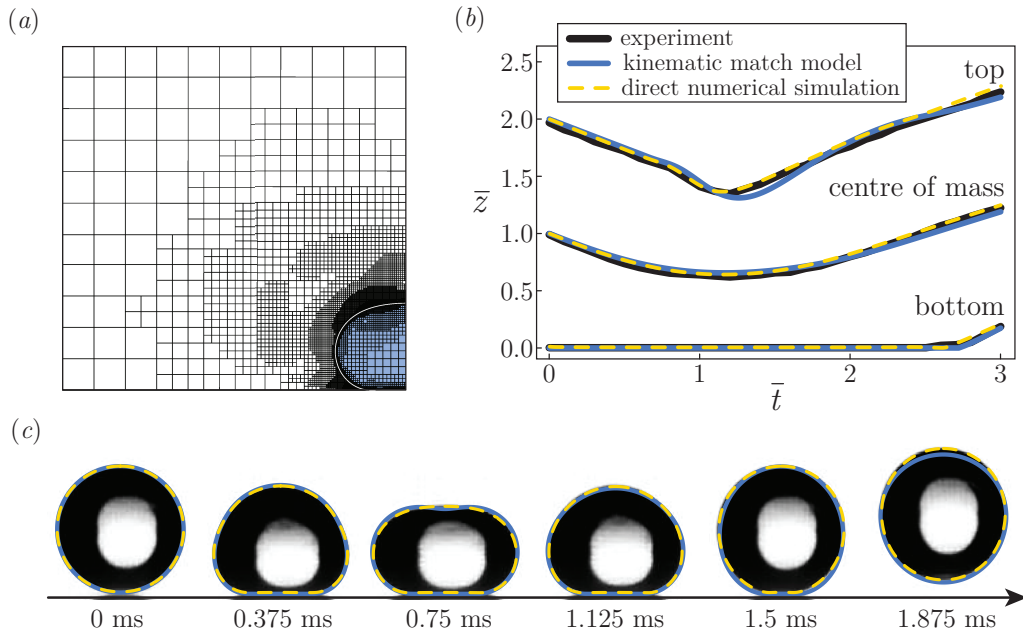


Figure 4: (a) Visualization of the computational domain comprising of liquid (blue) and gas regions (white), and underlying adaptive grid cell structure in the direct numerical simulation, for a typical $We = 0.253$ impact taken at the point of maximal radius deformation $t = 0.746$ ms. (b) Dimensionless distance above the substrate $\bar{z} = z/R$ against time $\bar{t} = t/t_\sigma$ for the top, bottom, and center of mass of a drop for $We = 0.253$, $Bo = 0.02$ and $Oh = 0.03$. Black solid lines represents experiment, while blue solid lines and yellow dashed lines represent the KM model and direct numerical simulations, respectively. (c) Overlay of the predicted shape from the KM model (solid blue) and direct numerical simulations (dashed yellow) with experimental images corresponding to (b). The drop radius is $R = 0.203$ mm and the time interval between images is 0.375 ms.

described in Section 3.1, and to interrogate quantities difficult to visualize experimentally. The fully nonlinear implementation is used to resolve the time-dependent Navier-Stokes equations in both liquid and gas phases, with physical properties of the latter taken to be the values of air at room temperature i.e. $\rho_g = 0.00121 \text{ g cm}^{-3}$ and $\mu_g = 0.000181 \text{ g cm}^{-1} \text{ s}^{-1}$, in an attempt to replicate the experimental conditions. Basilisk employs the volume-of-fluid method (Hirt & Nichols (1981); Scardovelli & Zaleski (1999)) for the implicit representation of the interface describing the transition between the different fluid regions, with a so-called color function f taking the value 1 inside the liquid and 0 inside the gas regions, respectively, and values $0 < f < 1$ representing computational cells cut by a fluid-fluid interface. The adaptive mesh refinement and parallelization capabilities of the implementation make it a particularly good candidate for this multi-scale impact problem. The code base for bouncing problems has been constructed and systematically validated for several years in our extended group, covering fluid-structure interaction (Galeano-Rios *et al.* 2021) and liquid-liquid impact (Alventosa *et al.* 2023), with comprehensive numerical campaigns in the wider community (Sanjay *et al.* 2023a,b) providing key insights into related regimes.

The axisymmetric computational domain set up in cylindrical coordinates measures $8R$ across both (r - and z -) spatial dimensions. To ensure sufficient resources are

dedicated to the delicate bouncing dynamics, we use a strong grid cell refinement level with a minimal grid cell size of approximately $1/20 \mu\text{m}$, verified to be robust across our parameter regime of interest. This stringent resolution specification was particularly relevant at the lowest Weber numbers studied herein, where the implementation requires most resilience in view of increased numerical stiffness. Adaptivity was tailored around the evolving location of the drop interface and changes in magnitude of the velocity components in the flow, as illustrated in figure 4(a). Special care was taken during runtime via stringent projection solver tolerances and increased number of internal iterations set for the multigrid cycle to ensure a high degree of accuracy. Furthermore, a zero Dirichlet boundary condition for the color function f was prescribed at the level of the solid surface to prevent touchdown and contact, with all tests resulting in the drop rebounding or resting on the surface. We employ a criterion based on the drop interface crossing a threshold level of $0.02R$ above the substrate to define the initialization and end of contact as discussed in Appendix A. This criterion enables us to build a consistent comparative framework with the model and experiment. Under these specifications, a typical run is characterised by $\mathcal{O}(10^5)$ grid cells and $\mathcal{O}(10 - 100)$ CPU hours of runtime, executed across multiple cores on local high-performance computing architectures. Mesh-independent results in our target metrics have been observed under the conditions above and reported in the sections to follow. All associated code, including setup scripts and post-processing functionality, are provided in the form of a GitHub repository at <https://github.com/rcsc-group/BouncingDropletsSolidSurface>.

3.3. Validation

Beyond verification and resolution studies across our parameter space of interest, we also validate our theoretical approaches with experimental data. A typical case illustrating a comparison between the kinematic match (KM) model and DNS is the rebound of a drop with radius $R = 0.203 \text{ mm}$ for $We = 0.253$, $Bo = 0.02$, and $Oh = 0.03$. Figure 4(b) plots the normalized distance from the substrate $\bar{z} = z/R$ of the top, bottom, and center of mass of the drop against time $\bar{t} = t/t_\sigma$. The experimental trajectory is shown in black and aligns well with predictions from the KM model (blue solid line) and DNS (yellow dashed line) for all three locations. Figure 4(c) shows overlays of the predicted drop shape from the KM model (solid blue line) and DNS (yellow dashed line) onto experimental images, demonstrating strong visual agreement. Supplemental movie 3 shows this rebound event with overlays. Additionally, we note that the accuracy of the KM model improves on a relative basis as We decreases, as demonstrated in supplemental movie 4 for a similar drop at $We = 0.023$. This low- We regime is of high consistency with the underlying simplifying assumptions, one in which resources can also be deployed very efficiently given smaller interface deformations. By contrast, we find that the DNS framework struggles for sufficiently low values of We (which we identified to be of $\mathcal{O}(10^{-2})$ or lower) without significant customization or computational re-design, as both numerical stiffness and parasitic capillary currents become progressively more difficult to contain accurately. This makes the cross-validation and interplay with the KM model even more constructive as our investigation reaches distinguished limits of our target parameter regime.

4. Results

We performed experiments over a wide range of We , Oh and Bo , as highlighted in supplemental movies 5, 6, and 7. In this section, we compare our results with direct numerical simulation data and the KM model. We first investigate the metrics defining

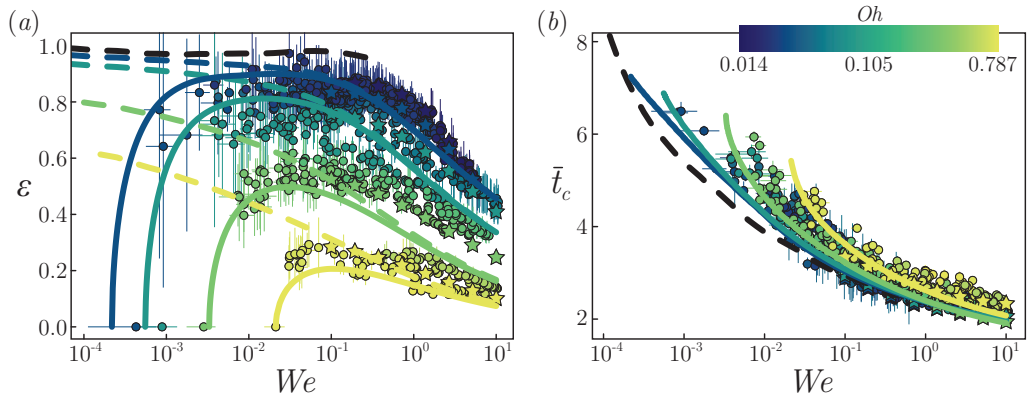


Figure 5: (a) Coefficient of restitution ε against Weber number We for drops with varying Oh . Circles denote experiments and stars represent DNS results for $Bo = 0.02$, a typical value in experiment. Solid and dashed lines are the KM model for $Bo = 0.02$ and $Bo = 0$, where the black dashed line shows the inertio-capillary limit ($Oh = 0; Bo = 0$). (b) Dimensionless contact time $\bar{t}_c = t_c/t_\sigma$ against We for experiments, DNS, and model predictions from (a). The color bar maps Oh to color on a logarithmic scale.

rebound, the coefficient of restitution ε and contact time t_c . Next, we analyze the evolution of the drop shape and timescales associated with spreading and retraction. Last, we show how the maximum deformation of the drop changes over our parameter space and compare with the KM model and energetic arguments.

4.1. Rebound metrics

The coefficient of restitution ε quantifies the energy recovered during rebound, and behaves differently at low and high We . Figure 5(a) shows ε against We , for various Oh spanning two orders of magnitude (as denoted by color). Here, circle markers represent experiments and star markers represent DNS results for $Bo = 0.02$, the most common value in our low- We experiments. The solid and dashed lines are predictions from the KM model for $Bo = 0.02$ and $Bo = 0$, respectively. The intercept of a curve with the x -axis signifies the cessation of rebound. The KM model predictions for the experimental trends at low We agree reasonably well with experiment and produce robust predictions even at very low We where the DNS struggles. At high We , the DNS predictions agree better with experiment, where the assumptions of the kinematic model are less justified. The complementary modeling approaches allows us to confidently span the full region accessed by experiment, and beyond.

For $We \gtrsim 0.5$, ε decreases as We increases for each Oh in agreement with prior literature (Biance *et al.* 2006; Jha *et al.* 2020). In addition, the black dashed line shows the prediction of the KM model in the strict inertio-capillary limit ($Oh = 0; Bo = 0$). Even in the complete absence of gravity and viscosity, our model predicts a similar roll-off at high We due to energy transfer to droplet oscillations not accounted for in the definition of ε . Curiously, this high- We roll-off is notably absent for the analogous case of droplet-bath rebounds, where for low Oh and Bo , the coefficient of restitution levels off at approximately 0.3 (Zhao *et al.* 2011; Wu *et al.* 2020; Alventosa *et al.* 2023).

Below $We \approx 0.5$, ε becomes nearly We -independent across roughly two orders of magnitude when Oh is small. As Oh increases, the influence of We on ε increases. As We decreases, Bo effects cause $\varepsilon \rightarrow 0$ at a critical Weber number We_c that increases with

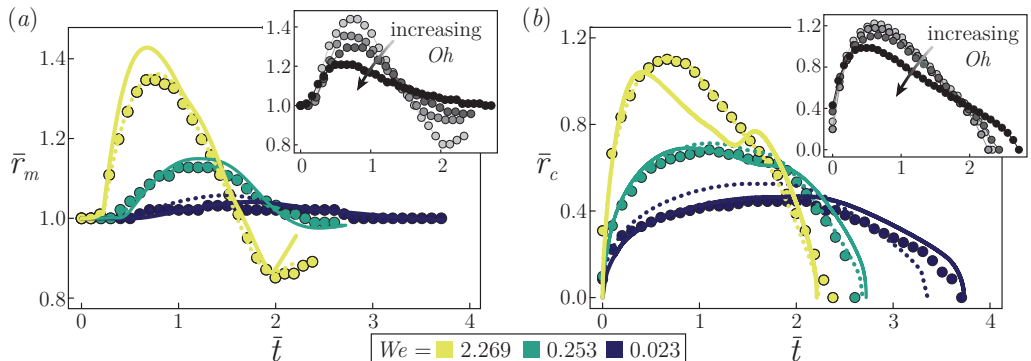


Figure 6: (a) Dimensionless equatorial radius $\bar{r}_m = r_m/R$ against dimensionless time $\bar{t} = t/t_\sigma$ for experiments (markers), DNS (dotted lines), and the KM model (solid lines) for $We = 2.269$ (light yellow), $We = 0.253$ (green), and $We = 0.023$ (dark blue), where $Bo = 0.02$ and $Oh = 0.03$ for all curves. (b) Dimensionless contact radius $\bar{r}_c = r_c/R$ against dimensionless time $\bar{t} = t/t_\sigma$, where line, marker type, and color are the same as (a). The insets show experimental results for drops of similar We (2.5 – 3.5) and Bo (0.16 – 0.24) for $Oh = 0.03, 0.08, 0.29$, and 0.7 , where marker darkness indicates higher Oh .

Oh . For the experimental data presented, $\varepsilon = 0$ represents the highest We experiment where rebound was not detected (for each viscosity). In related work for low We rebound on hydrophobic surfaces, a similar roll-off leading to bounce cessation was attributed to contact line friction (Wang *et al.* 2022; Thenarianto *et al.* 2023), wholly absent in the current experiments and models. To investigate the physical origin of this threshold in our fully non-wetting scenario, we performed additional KM simulations in the absence of gravity (i.e. $Bo = 0$, shown as the colored dashed curves). For the parameters considered here, We_c is eliminated in the absence of gravity, effectively extending bouncing to lower We . Gravity shifts the static equilibrium height of the drop's center of mass below one radius above the surface, representing a higher barrier for complete rebound when energy is lost to viscosity or transferred to droplet oscillations during contact. In the low We regime, the KM model predicts nearly perfect elastic collisions ($\varepsilon \approx 1$) in the inertio-capillary limit ($Oh = 0$; $Bo = 0$).

The contact time t_c follows the simple scaling $t_c \sim t_\sigma$ for moderate and high We (Richard *et al.* 2002) but depends on We and Oh at low We . Figure 5(b) shows the nondimensional contact time $\bar{t}_c = t_c/t_\sigma$ against We for drops of varying Oh . The results correspond with those in figure 5(a); thus, plot markers, line types, and colors hold the same meaning. For all Oh , the contact time approaches a constant as We increases, in agreement with prior literature (Okumura *et al.* 2003). As We decreases, t_c increases at an Oh -dependent rate; the rate of increase is greater for larger Oh . Thus, the effects of viscosity on contact time are most influential at low We and may alter the utility of drops in a number of applications involving heat transfer (Shiri & Bird 2017), for instance. The KM model agrees well here for all We and Oh , and the inertio-capillary limit sets a lower bound on the contact time and an upper bound on the coefficient of restitution for each We , similar to the case for droplet-bath rebound (Alventosa *et al.* 2023).

4.2. Spreading and retraction

The shift in rebound behavior between low and high We revealed in § 4.1 coincides with a shift in the spreading and retraction dynamics. Figure 6(a) shows the non-dimensional equatorial radius $\bar{r}_m = r_m/R$ against non-dimensional time $\bar{t} = t/t_\sigma$ during contact for $We = 0.023$ (dark blue), $We = 0.253$ (green), and $We = 2.269$ (light yellow), with $Bo = 0.02$ and $Oh = 0.03$. Circles represent experimental measurements, while dotted and solid lines denote DNS and the KM model results, respectively. In all cases, inertia drives spreading, causing \bar{r}_m to increase after an initial period of localized deformation where $\bar{r}_m \approx 1$. As We increases, the drop expands quicker and \bar{r}_m reaches a higher maximum. After the drop reaches its maximum extent, surface tension drives retraction, decreasing \bar{r}_m . For $We = 0.023$, retraction mirrors spreading, and \bar{r}_m evolves symmetrically, consistent with quasi-static-like behavior (Moláček & Bush 2012; Chevy *et al.* 2012). When $We = 2.269$, the two phases are dissimilar, and \bar{r}_m overshoots $\bar{r}_m = 1$ during retraction, leading to apparent underdamped oscillations. The inset plot shows the evolution of \bar{r}_m for drops of similar We and Bo but varying Oh , where darker marker shade indicates higher Oh . Increasing viscous dissipation can eliminate the appearance of underdamped behavior; however, it is not sufficient to recover the symmetry between spreading and retraction. Instead, higher Oh shortens the spreading phase, reduces the maximum \bar{r}_m , and lengthens the retraction phase, thereby increasing asymmetry in the spreading and retraction process.

The increased asymmetry between spreading and retraction as We increases is also observed in the nondimensional contact radius $\bar{r}_c = r_c/R$. Figure 6(b) shows $\bar{r}_c = r_c/R$ against nondimensional time $\bar{t} = t/t_\sigma$ for $We = 0.023$ (dark blue), $We = 0.253$ (green), and $We = 2.269$ (light yellow). The data and model predictions correspond with those in figure 6(a); thus, plot markers, line types, and colors hold the same meaning. Unlike \bar{r}_m , there is no delay in the response of \bar{r}_c to impact as $\bar{t} = 0$ is defined as the moment the drop and substrate “contact”. As We increases, the maximum \bar{r}_c increases, while the time to reach it decreases. For $We = 0.023$, the spreading and retraction of \bar{r}_c are symmetric, whereas at $We = 2.269$, they are asymmetric, qualitatively resembling the behavior of \bar{r}_m during rebound. The inset shows the evolution of \bar{r}_c for drops of similar Bo and We , but increasing Oh , as indicated by darker shaded markers. Similar to \bar{r}_m , increasing Oh shortens the spreading phase by reducing the maximum \bar{r}_c , and extending the retraction phase. The asymmetry between spreading and retraction motivates a detailed look at their relationship across all experiments.

The spreading time t_s is the time from when the drop first contacts the substrate until r_c reaches its maximum value R_c , and is proportional to the retraction time t_r at low We . In figure 7 we show the relative spreading time t_s/t_c , where the contact time is the sum of the spreading and retraction time $t_c = t_s + t_r$, against We for all Oh . Solid lines represent predictions from the KM model for $Bo = 0.02$, with the black dashed curve representing the inertio-capillary limit ($Bo = 0$; $Oh = 0$). When $We \gtrsim 0.5$, drops spread faster than they retract, and increasing We increases the difference between t_s and t_r . However, the time the drop spends spreading relative to retracting is nearly We -independent for $We \lesssim 0.5$, until the drop ceases to bounce. This trend holds for all viscosities, with Oh limiting the maximum of t_s/t_c . Although this maximum approaches 0.5 as $We \rightarrow 0$ in the inertio-capillary limit, it surpasses it and peaks near $We = 0.04$. The inset in figure 5 shows the evolution of the dimensionless contact radius \bar{r}_c near its maximum, which is denoted by a black dot. Oscillations due to capillary waves cause an apparent jumpiness in t_s at low Oh . In particular, as We decreases from $We = 0.05$ to $We = 0.04$, the maximum contact radius suddenly switches between its two largest peaks, producing the

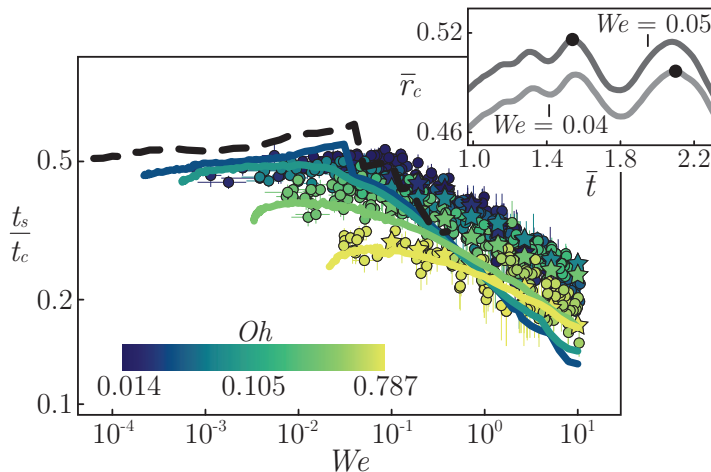


Figure 7: The relative spreading time t_s/t_c against Weber number We for drops with varying Oh . Circles represent experiment and stars denote DNS for $Bo = 0.02$. Solid lines are predictions from the KM model for $Bo = 0.02$, and the black dashed line shows the inertio-capillary limit ($Oh = 0$; $Bo = 0$). The inset shows the predicted dimensionless contact radius \bar{r}_c against dimensionless time $\bar{t} = t/t_\sigma$ for $We = 0.04$ and $We = 0.05$, where $Bo = 0$ and $Oh = 0$. The black dots show when \bar{r}_c is maximum.

apparent sudden rise in t_s . These results reveal that the symmetry of the spreading and retraction process coincides with nearly-elastic rebound metrics that are independent of We in the inertio-capillary limit. In contrast, the emergence of asymmetry coincides with the onset of We -dependent trends for ε while increasing Oh similarly decreases t_s/t_c and ε across all We . As in the prior rebound measurements, the KM model performs best for low We whereas the DNS excels at higher We for the spreading and retraction metrics presented throughout this section.

4.3. Maximum spreading and deformation

We next examine how drop deformation depends on the governing dimensionless parameters and relate deformation and spreading. To do this, we define the maximum equatorial deformation $\beta - 1$, where $\beta = R_m/R$ is the nondimensional maximum equatorial radius and $R_m = \max(r_m(t))$. Similarly, we define maximum vertical deformation $1 - \alpha$, where $\alpha = H_{min}/2R$ and $H_{min} = \min(H(t))$. Lastly, we define the maximum spreading radius as $\beta_c = R_c/R$, where $R_c = \max(r_c(t))$.

4.3.1. Energy argument

In addition to the kinematic match model, we can compare the drop spreading and deformation to a simpler energetic argument by assuming the drop principally deforms in the $l = 2$ mode in the low- We regime. Under this assumption, the instantaneous drop shape is fully defined by the coefficient \mathcal{A}'_2 , with $r_m = R - \frac{1}{2}\mathcal{A}'_2$ and $h = 2R + 2\mathcal{A}'_2$.

The anomalous surface energy associated with drop deformations of the l -th mode (for $l \geq 2$) can be expressed as

$$E_l = 2\pi\sigma \frac{(l+2)(l-1)}{2l+1} \mathcal{A}_l'^2, \quad (4.1)$$

with the surface energy in the $l = 2$ mode being $E_2 = \frac{8}{5}\pi\sigma \mathcal{A}_2'^2$ (Moláček & Bush 2012).

Neglecting gravity ($Bo^2 \ll We$) and viscous dissipation ($Oh \ll 1$), and assuming the initial kinetic energy of the droplet ($E_V = \frac{2}{3}\pi\rho R^3 V^2$) is fully converted into surface energy of the $l = 2$ mode (i.e. $E_V = E_2$), one finds

$$\beta - 1 = \sqrt{\frac{5}{48}} We^{1/2} \quad (4.2)$$

and

$$1 - \alpha = \sqrt{\frac{5}{12}} We^{1/2}, \quad (4.3)$$

using the relations $\mathcal{A}'_2 = 2R(1 - \beta)$ and $\mathcal{A}'_2 = R(\alpha - 1)$, respectively, and assuming $\mathcal{A}'_2 \leq 0$ (i.e. $R_m \geq R$, $H_{min} \leq 2R$) in the deformed state. The result for $\beta - 1$ (equation 4.2) is identical to that derived by Richard & Qu  r   (2000) using similar arguments. This derivation also suggests a geometric relationship between β and α :

$$1 - \alpha = 2(\beta - 1). \quad (4.4)$$

To connect this deformation to the contact radius r_c , we appeal to a quasi-static argument expected to be valid for $We \ll 1$ (Chevy *et al.* 2012; Mol    ek & Bush 2012). The force associated with the creation of additional surface area in the $l = 2$ mode can be expressed as the derivative of the surface energy, $F_2 = -\frac{dE_2}{d\mathcal{A}'_2} = -\frac{16}{5}\pi\sigma\mathcal{A}'_2$. Following Chevy *et al.* (2012), we assume small deformations such that the capillary pressure inside the drop is approximately $2\sigma/R$, and thus the net vertical force associated with the ‘contact’ region is $F_\sigma = \frac{2\sigma}{R}\pi r_c^2$. Balancing these forces, one arrives at the relationship $\frac{r_c^2}{R^2} = -\frac{8}{5}\frac{\mathcal{A}'_2}{R}$. This result can be combined with the prior relations to arrive at the prediction

$$\beta_c^2 = \frac{16}{5}(\beta - 1) \quad (4.5)$$

or

$$\beta_c = \left(\frac{16}{15}\right)^{1/4} We^{1/4}. \quad (4.6)$$

Note that equations (4.2)–(4.6) have limited predictive power compared with the KM model, which captures viscous effects and the complete evolution of the drop shape. Nevertheless, the favorable comparison between the simple energy argument and KM model elucidates the dominant mode of deformation and motivates the parametric scalings.

4.3.2. Comparisons

Figure 8(a) shows the maximum equatorial deformation $\beta - 1$ against Weber number We for all experiments (circles) and DNS (stars). Predictions from the KM model are shown as solid lines for $Bo = 0.02$, with the black dashed curve showing the inertio-capillary limit ($Oh = 0$; $Bo = 0$). The maximum deformation $\beta - 1$ monotonically increases with We and is well captured by the KM model. The red dot-dashed curve is equation (4.2), which gives an excellent prediction for our low-viscosity ($Oh < 0.05$) data with no fitting parameters. This agreement persists across four orders of We , as shown more clearly in the inset with our low-viscosity results and data from prior literature (Okumura *et al.* 2003; Clanet *et al.* 2004; Biance *et al.* 2006; Laan *et al.* 2014). Beyond $We \approx 10^2$, equation (4.2) no longer captures the trend of the amalgamated data, which follows a trend more closely resembling $\beta - 1 \sim We^{1/4}$.

The maximum vertical deformation $1 - \alpha$ can also be accurately predicted by our KM model and energy arguments. Figure 8(b) shows $1 - \alpha$ against Weber number We

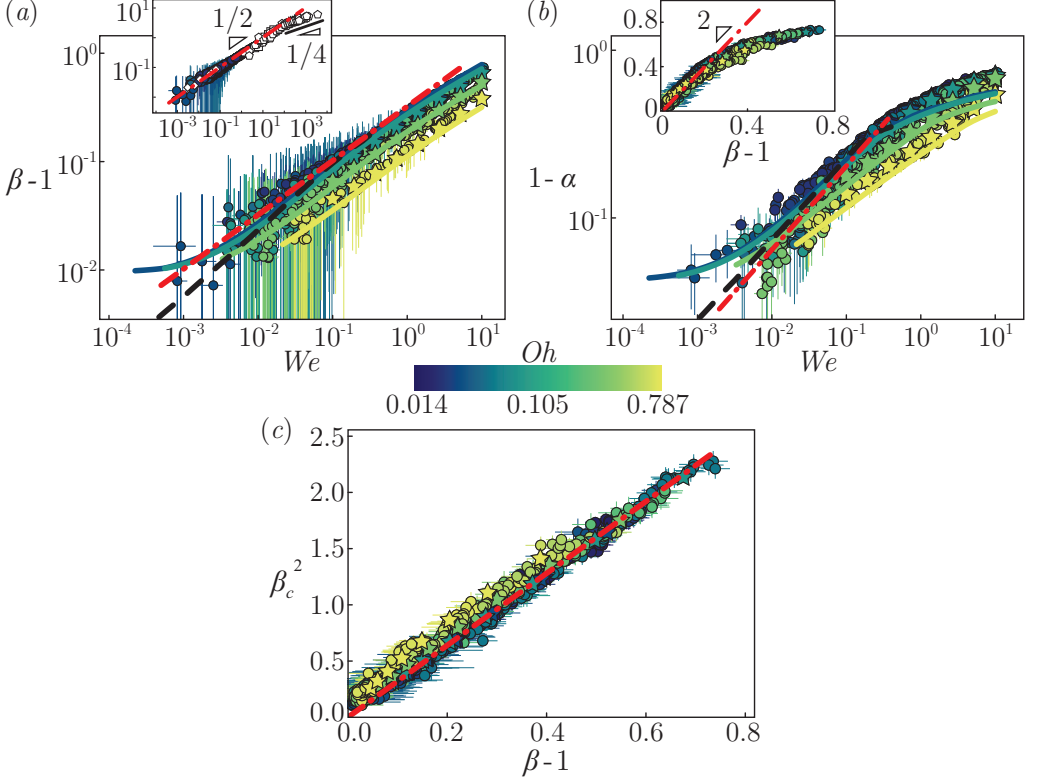


Figure 8: (a) Maximum equatorial deformation $\beta - 1$ ($\beta = R_m/R$) and (b) maximum vertical deformation $1 - \alpha$ ($\alpha = H_{min}/2R$) plotted against Weber number We . Circles represent experiment and stars denote DNS for $Bo = 0.02$. Solid curves show the KM model with $Bo = 0.02$, and the inertio-capillary limit ($Oh = 0$; $Bo = 0$) is represented by black dashed curves. The red dot-dashed curves are predictions from our simplified model (§ 4.3.1). The inset in (a) shows our low-viscosity data $Oh < 0.05$ (colored circles) with prior results (diamond (Okumura *et al.* 2003), pentagon (Clanet *et al.* 2004), square (Biance *et al.* 2006), triangle (Laan *et al.* 2014)). The red dot-dashed curve is equation (4.2), and the black solid line with slope 1/4 is used to guide the eye. The inset in (c) plots $1 - \alpha$ against $\beta - 1$ for all experiments and the red dot-dashed curve is equation (4.4). (c) Dimensionless spreading area β_c^2 against $\beta - 1$ for all experiments and DNS results, with equation (4.5) shown as a red dot-dashed curve. The color bar maps Oh to color on a logarithmic scale.

for all experiments (circles) and DNS (stars). The KM model is shown as solid lines for $Bo = 0.02$, and the black dashed line denotes the inertio-capillary limit ($Oh = 0$; $Bo = 0$). The red dot-dashed line is equation (4.3). For low Oh and We , the data follows a power-law trend captured by the KM model and energy argument, but flattens when $We \gtrsim 0.5$ due to self-occlusion of the drop surface, a result of our definition for H , and because $1 - \alpha$ must eventually saturate to 1. The KM model and DNS results capture this feature for all Oh , closely following experimental results. As Oh increases, $1 - \alpha$ decreases and follows a weaker power-law trend. Additionally, self-occlusion is delayed to larger We or disappears altogether for our largest Oh . The inset in figure 8(b) shows $1 - \alpha$ against $\beta - 1$ for all experiments and DNS. The data follows the linear trend predicted

by equation (4.4) for $\beta - 1 \lesssim 0.3$. At higher deformations, the data continues to follow a single trend, but necessarily deviates from the energy argument since the deformations are no longer small and $1 - \alpha$ must saturate to unity.

The maximum spreading radius β_c is a key parameter in determining the heat transfer and total interaction between a drop and substrate in many applications. When $We > 1$, an impacting drop flattens into a pancake-like shape, such that $\beta_c \approx \beta - 1$, making $\beta - 1$ a convenient and practical proxy for β_c . This is invalid at low We , and necessitates a revised relationship between β_c and β . From our energy argument, equation (4.5) predicts a linear relationship between the maximum drop deformation and maximum spreading area β_c^2 . Figure 8(c) plots β_c^2 against $\beta - 1$ for all experiments (circles) and DNS (stars), with equation (4.5) overlaid as a red dot-dashed curve. Strikingly, this prediction is accurate across all dimensionless parameters explored, and provides a simple relationship connecting drop spreading and deformation in the low We regime.

5. Discussion

Previous attempts to quantify rebound behavior for $We < 1$ used superhydrophobic substrates, where contact line friction altered and ultimately suppressed rebound (Wang *et al.* 2022; Thenarianto *et al.* 2023). We overcame this limitation by using a thin viscous film as the substrate, which allowed rebound at as low as $We = 0.0008$. Additionally, we provide the first systematic study of the role of Oh for $We < 1$ rebounds. Our main finding is a transition to unique trends in the rebound metrics—the coefficient of restitution ε and contact time t_c —at low We . These trends were shown to coincide with a change in the spreading and retraction dynamics, which become symmetric in the inertio-capillary limit, leading to nearly elastic rebound. We complemented these findings with reduced-order models formulated to describe low- We rebound, and show that they provide accurate predictions for the rebound metrics, drop deformation, and drop spreading.

The coefficient of restitution ε and contact time t_c have different We -dependencies at low and high We . When $We \gtrsim 0.5$, the coefficient of restitution ε decreased as We increased, as observed in prior studies (Biance *et al.* 2006; Jha *et al.* 2020). When $We \lesssim 0.5$, ε reached a maximum that depends upon Oh and Bo , and becomes We -independent in the inertio-capillary limit. A gravity-induced roll-off in ε leading to $\varepsilon \rightarrow 0$ is the natural route to rebound suppression when Bo is finite, with Oh increasing the critical Weber number We_c below which rebound stops. These results differ from the peak and subsequent roll-off in ε as We decreases reported for $We < 1$ rebounds on superhydrophobic substrates (Richard & Quéré 2000; Wang *et al.* 2022; Thenarianto *et al.* 2023). Although these prior experiments were conducted in low Oh conditions, and in some cases used low Bo drops, the increased effect of contact line friction at low We was shown to be the primary mechanism for rebound suppression. Consequently, our results show that submillimeter drops, like those from coughing (Dbouk & Drikakis 2020) or agricultural sprays (Kooij *et al.* 2018; Makhnenko *et al.* 2021; Chen & Ashgriz 2022), may continue bouncing longer than previously thought when the substrate is non-wetting—an important insight into the spread of their contents. The contact time between the drop and substrate is We -dependent at low We (Foote 1975; Okumura *et al.* 2003), and our results show that it is also Oh -dependent in this regime. Increasing Oh , causes t_c to increase at a higher rate as We decreases such that viscosity is most influential on t_c in the low- We regime. Since t_c is a critical parameter governing drop–substrate interaction in various applications Shiri & Bird (2017); Díaz *et al.* (2022), this finding

has immediate practical implications, and motivates the study of low We rebound using drops with shear-dependent viscosity in future work.

In section 4.2, we compared the drop shape during spreading and retraction for three values of We spanning the transition from low We to high We , and revealed a nearly symmetric spreading and retraction process for low Oh , low We rebound. As We increased, the spread time decreased relative to the retraction time, increasing asymmetry between spreading and retraction and aligning with the changes in rebound behavior. This change corresponds to a loss of energy during rebound when $We > 1$ and was investigated through a careful energy budget analysis by Gilet & Bush (2012). Their results showed that when $We < 1$, the initial translational energy was efficiently converted to surface energy during the spreading phase. When $We > 1$, this conversion was inefficient, with an appreciable loss of energy during spreading. This suggests that the time symmetry is broken in the spreading phase at high We . Additionally, Bartolo *et al.* (2005) identified a limit on the retraction rate of a drop that is substrate-independent for low Oh . Although this limit does not explain the onset of asymmetry, which requires considering the energy lost during spreading, it helps rationalize how the spreading-to-retraction time ratio evolves as We increases when $We > 1$. In our experiments, this ratio follows the scaling $t_s/t_r \sim We^{-0.26 \pm 0.01}$ in the low Oh limit. We can rationalize this observation by considering the inertio-capillary limit, where the time needed for a drop to spread $t_s \sim R_c/V$, where $R_c \sim RWe^{-1/4}$ from our energy argument (4.6), and the maximum retraction rate $t_r^{-1} \sim t_\sigma^{-1}$ (Bartolo *et al.* 2005). This analysis gives $t_s/t_r \sim We^{-1/4}$, in good agreement with our results. We therefore interpret the growing asymmetry in rebound dynamics at $We > 1$ as the result of two effects: a loss of energy during spreading that breaks time symmetry early in the rebound process (Gilet & Bush 2012), and a limited retraction rate that further skews the rebound timescale (Bartolo *et al.* 2005). Recent studies have also noted the near-symmetry between spreading and retraction times low We (Lin *et al.* 2024). Our results confirm and extend this observation, by demonstrating that time symmetry holds in the inertio-capillary regime and is progressively lost as either We or Oh increases.

Lastly, we examined the drop deformation and spreading in section 4.3, and showed that the KM model captures drop deformation well across a wide range of Oh , and agrees with a simple energy model in the low Oh limit, indicating that deformation is primarily in the $l = 2$ mode. The literature on the maximum horizontal deformation is vast and two competing scaling arguments have gained support: one based on momentum conservation $\beta \sim We^{1/4}$ (Clanet *et al.* 2004; Bartolo *et al.* 2005; Biance *et al.* 2006; Tsai *et al.* 2011; García-Geijo *et al.* 2020) and the other arising from energy conservation $\beta \sim We^{1/2}$ (Chandra & Avedisian 1991; Bennett & Poulikakos 1993; Okumura *et al.* 2003; Eggers *et al.* 2010; Villiermaux & Bossa 2011; Laan *et al.* 2014; Lee *et al.* 2016). Despite extensive efforts, the correct scaling remains debated, in part due to most studies using the maximum equatorial radius $\beta = R_m/R$ to describe horizontal deformation. However, as discussed in (Josserand & Thoroddsen 2016), β ignores the initial drop radius and is inadequate to discern scaling arguments at low We . In this work we used the maximum equatorial deformation $\beta - 1$, and energy arguments predict $\beta - 1 = (5/48)^{1/2} We^{1/2}$, as in Richard & Quéré (2000). This prediction is in excellent agreement with our low Oh data and requires no fitting parameters. Furthermore, we combined our low Oh data with that from previous studies and validated equation (4.2) from $We = 10^{-4}$ to $We = 10^2$, above which the data begins following a trend closer to $\beta - 1 \sim We^{1/4}$. As Oh increases, (4.2) is less accurate; however, the KM model continues to provide accurate predictions. The KM model also captures the maximum vertical

deformation $1 - \alpha$ across all Oh , and our energy argument (equation (4.3)) provides a simple and accurate prediction when Oh and Bo effects are negligible. In addition to relating vertical and horizontal deformation, our energy argument allows us to relate maximum deformation and spreading. For example, equation (4.5) predicts a linear relationship between the horizontal deformation and maximum spread area β_c^2 , which holds for all Oh and Bo tested. This relationship provides a useful tool for determining the contact area of a bouncing drop from its deformation, which is critical for applications such as heat transfer (Shiri & Bird 2017) or predicting the net charge acquired by a rebounding water drop (Díaz *et al.* 2022).

6. Conclusions

We studied a drop rebounding from a non-wetting, rigid substrate at low We using experiments, direct numerical simulation, and reduced-order modeling. We revealed the rebound behavior of drops at low We for a range of Oh , showed how increasing Oh or We breaks the symmetry between the spreading and retraction phases, and elucidated the critical role of Oh and Bo in suppressing rebound. The maximum drop deformation and spreading were connected through energy arguments, and closely followed the predictions of the KM model irrespective of Oh . These findings reveal new physical insight into drop rebound and provide practical tools for predicting drop deformation on non-wetting substrates.

The interplay between our theoretical approaches, the KM model and the dedicated direct numerical simulation setup, enabled us to cross-validate these tools and establish the range of validity of the reduced-order model with a significant level of confidence, with the experimental dataset acting as foundation where comparisons were possible. Thus, we were suitably equipped to use the more efficient methodology in the relevant section of the parameter space and relevant distinguished limits thereof, while also being able to rely on DNS for larger values of We where the model assumptions no longer hold. In general, DNS is preferable for $We > 1$, while the reduced-order model offers high-accuracy predictions with substantially lower computational cost for $We < 1$, but continues to yield reasonable estimates up to $We \approx 10$. Furthermore, our work also presents the first application of the kinematic match method to the case of a deformable impactor rebounding off a rigid substrate. The quality of the resulting predictions highlights its versatility and naturally invites further applications for it; e.g., its use in the case of a collision of two deformable objects, and in combination with moving meshes and variational methods.

When contact line formation is avoided, the coefficient of restitution ε is We -independent at low We in the inertio-capillary limit. Finite Bo effects suppress bouncing while increasing Oh decreases ε and increases the critical Weber number We_c where rebound ceases. In contrast, the contact time t_c increases as We decreases at a rate that increases with Oh . The shift in how ε and t_c change with We in the low We and high We regimes coincides with altered spreading and retraction dynamics. In particular, the nearly elastic rebound observed in the inertio-capillary limit have a nearly-symmetric spreading and retraction phase, but increasing We above unity and increasing Oh decreases ε and increases asymmetry in the spreading and retraction process. Using energy arguments, we derive simple equations that accurately predict the maximum vertical and horizontal deformation, and the maximum spreading for low Oh impacts with no fitting parameters. The prediction for the maximum horizontal deformation (4.2) reveals that the horizontal deformation of an impacting drops scales as $We^{1/2}$, which when compared with experimental data holds up to $We \approx 10^2$. Additionally, this simple model accurately relates $\beta - 1$ to the maximum vertical deformation $1 - \alpha$

via equation (4.4) and maximum contact area β_c^2 via equation (4.5). For all Oh , the kinematic match model provides excellent predictions for the maximum spreading and deformation for low We rebound where direct numerical simulation struggles due to numerical stiffness and parasitic capillary currents.

Although we focus here on the normal impact of a drop on a rigid surface, the ubiquity of drop impacts make our findings relevant to many situations. For example, low- We rebound governs the final stage of drop dispersal in many applications involving low- Bo drops, such as agricultural sprays (Kooij *et al.* 2018; Makhnenko *et al.* 2021; Chen & Ashgriz 2022) and cough ejecta (Dbouk & Drikakis 2020; Bourouiba 2021), where understanding the spread of the drops contents is essential. In both examples, the drops typically impact non-wetting surfaces, as plant leaves are often naturally superhydrophobic (Barthlott & Neinhuis 1997), while medical surfaces are frequently rendered superhydrophobic to reduce microbial adhesion and biofluid contamination (Falde *et al.* 2016). Future work is needed to extend our results to more complex practical and natural settings, which often involve non-Newtonian drops and complaint substrates that have a pronounced effect on drop impact at high We (Bartolo *et al.* 2007; Basso & Bostwick 2020) but remain unexplored for drop rebound at low Weber number. Furthermore, our focus herein has been strictly on the liquid dynamics whereas the coupled air layer dynamics are also a source of rich physics, and have become of increasing interest to modelers Phillips & Milewski (2024); Sprittles (2024).

Supplementary movies.

Supplementary movies are available at
<https://github.com/harrislab-brown/LowWeberDropRebound>.

Supplementary material.

The kinematic match code, supplemental movies, and data used in each figure are available at <https://github.com/harrislab-brown/LowWeberDropRebound>. The direct numerical simulation code infrastructure, including pre- and post-processing functionality and a short descriptive tutorial, can be found at
<https://github.com/rcsc-group/BouncingDropletsSolidSurface>.

Funding.

The authors gratefully acknowledge the financial support of the National Science Foundation (NSF CBET-2123371) and the Engineering and Physical Sciences Research Council (EPSRC EP/W016036/1). C.T.G. gratefully acknowledges the Hope Street Fellowship for financial support.

Declaration of Interests.

The authors report no conflict of interest.

Data accessibility.

All data reported in this study is available at
<https://github.com/harrislab-brown/LowWeberDropRebound>.

Appendix A. Defining contact

Determining the substrate location is crucial for evaluating drop–substrate interactions. However, this is typically constrained by the spatial resolution of the measurement technique. In this study, the presence of an intervening air layer further complicates identifying the substrate, as it prevents direct contact with the drop. In our experiments the spatial resolution related to the pixel width in our images was approximately $0.02R$, which can lead to discrepancies when compared with KM model and simulation results if not considered. Figure 9(a) shows a drop impacting a substrate with a magnified view of the contact boundary. Increasing the substrate location by the spatial resolution of $0.02R$ (gray dashed line) shifts the true contact point (open circle) to the perceived contact point (solid circle), expanding the contact radius by an amount b and necessitating careful criteria for faithfully comparing experimental and modeling results. The non-wetting nature of the surface makes this process particularly sensitive due to the tangency with the substrate.

To provide the most accurate predictions between the KM model, DNS, and experiments, the former two measure all relevant variables using a hypothetical substrate located $0.02R$ above the true substrate. This criteria also allows DNS measurements to be made above the intervening air layer, which would otherwise need to be accounted for during post-processing. The parameters most affected by this criterion are the contact time, t_c , and contact radius, r_c , which both increase as a result. To show the magnitude of this effect, we plot the dimensionless contact time t_c/t_σ against We for the KM model with (gray lines) and without (black lines) the $0.02R$ criteria in figure 9(b), where solid lines represent $Bo = 0.019$ and dashed lines are for $Bo = 0$. The influence of the threshold increases as We decreases. Figure 9(c) shows the KM model for the dimensionless maximum contact radius $\beta_c = R_c/R$ versus We for the same threshold values. Again, the threshold effect increases as We decreases; however, unlike contact time, noticeable differences in the predictions persist even for $We > 1$.

By employing a discretized angular mesh for the polar coordinate, only a finite number of contact radii are numerically allowed. As a consequence, the $0.00R$ criterion predicts piecewise constant functions for the contact radius r_c , while the $0.02R$ criterion smooths this discretized behavior and results in smoother curves, as seen in figure 9(c).

We also compare these predictions to results obtained using the quasi-static model of Chevy *et al.* (2012). Their work predicts contact time t_c , but additional features about the shape, such as the contact radius r_c , are also extractable by reproducing their calculations. In figures 9(b,c), the red curves show predictions from Chevy *et al.* (2012)’s model with the solid line for $Bo = 0.019$ and dashed line for $Bo = 0$. While their modeling approach differs, their low- We predictions align very well with ours, but the KM model is able to make predictions above $We \approx 10^{-1}$ while also enforcing the natural geometric constraints in the contact region at all points.

Appendix B. Numerical approximations

B.1. The spectral method

We define A_l , U_l , B_l , \mathbf{h} and \mathbf{v} as approximations of \mathcal{A}_l , \mathcal{U}_l , \mathcal{B}_l , h and v , respectively. These represent the solutions to the system equations obtained by truncating the expansions of the surface shape, velocity and pressure distribution in spherical harmonics up to the L^{th} mode. That is

$$\dot{A}_l = U_l, \quad \text{for } l = 2, \dots, L; \quad (\text{B } 1)$$

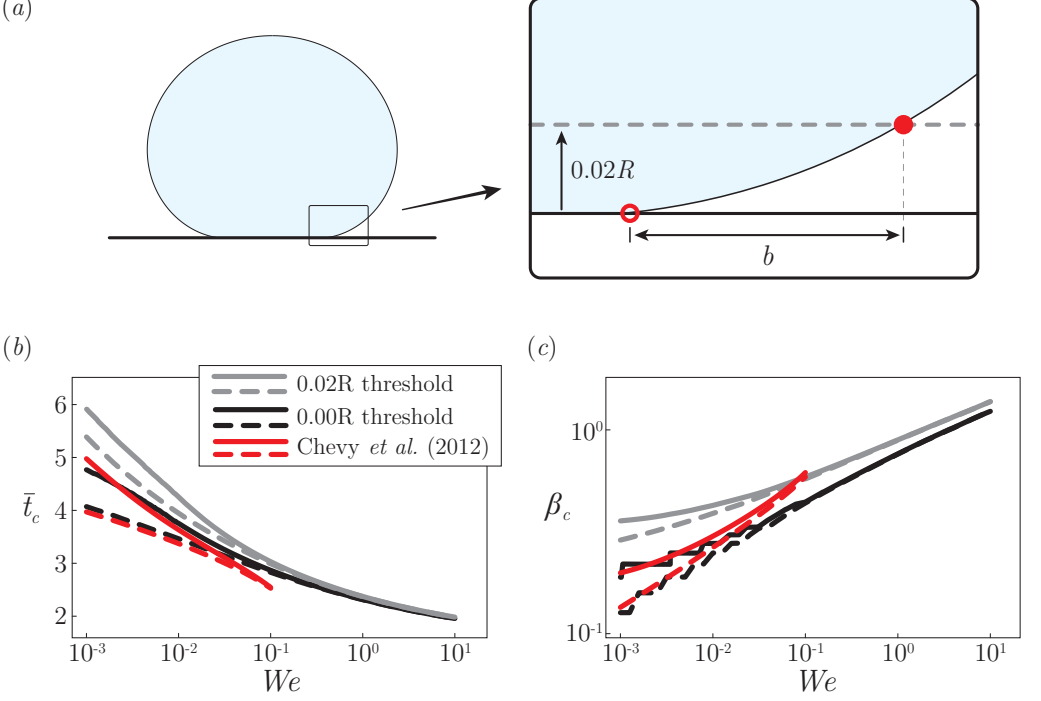


Figure 9: (a) Magnified view near a drop's contact point during impact. The hollow circle indicates the contact point with the substrate, while the filled circle marks the contact point along a hypothetical substrate at a height corresponding to the experimental spatial resolution $z = 0.02R$. This threshold increases the contact time and expands the contact radius r_c by b . (b) Dimensionless contact time $\bar{t}_c = t_c/t_\sigma$ and (c) dimensionless maximum contact radius $\beta_c = R_c/R$ against Weber number for the KM model evaluated at the hypothetical substrate $0.02R$ (gray) and true substrate $0.00R$ (black) for $Oh = 0.03$. Red curves represent predictions from the model of Chevy *et al.* (2012). Solid lines show predictions for $Bo = 0.019$, and dashed lines show results obtained for $Bo = 0$.

$$\dot{U}_l = -l(l+2)(l-1)A_l - 2(2l+1)(l-1)Oh U_l - lB_l, \quad \text{for } l = 2, \dots, L; \quad (\text{B } 2)$$

$$\dot{\mathbf{h}} = \mathbf{v}; \quad (\text{B } 3)$$

$$\dot{\mathbf{v}} = -Bo + B_1; \quad (\text{B } 4)$$

which are subject to

$$A_l(t=0) = 0, \quad \text{for } l = 2, \dots, L; \quad (\text{B } 5)$$

$$U_l(t=0) = 0, \quad \text{for } l = 2, \dots, L; \quad (\text{B } 6)$$

$$\mathbf{h}(t=0) = 1; \quad (\text{B } 7)$$

$$\mathbf{v}(t=0) = -\sqrt{We}; \quad (\text{B } 8)$$

$$\sum_{l=2}^L A_l P_l(\cos(\theta)) = \frac{\mathbf{h}}{\cos(\theta)} - 1, \quad \text{for } \theta \leq \theta_c; \quad (\text{B } 9)$$

$$\sum_{l=2}^L A_l P_l(\cos(\theta)) > \frac{\mathbf{h}}{\cos(\theta)} - 1, \quad \text{for } \theta > \theta_c; \quad (\text{B } 10)$$

$$\sum_{l=0}^L B_l P_l(\cos(\theta)) = 0, \quad \text{for } \theta > \theta_c; \quad (\text{B } 11)$$

$$\frac{\partial}{\partial \theta} \left[\left(1 + \sum_{l=2}^L A_l P_l(\cos(\theta)) \right) \cos(\theta) \right]_{\theta=\theta_c} = 0. \quad (\text{B } 12)$$

For the present work, calculations were performed using $L = 90$ spherical modes. Convergence was verified by testing resolutions of 120, confirming that all quantities of interest varied by less than 10% across the full dimensionless parameter range—representing the worst-case deviation—with an average relative error below 5%.

B.2. Finite differences in time

We approximate the time derivatives by defining $A_l^k \approx A_l(t = t^k)$, $U_l^k \approx U_l(t = t^k)$, $B_l^k \approx B_l(t = t^k)$, $h^k \approx \mathbf{h}(t = t^k)$, $v^k \approx \mathbf{v}(t = t^k)$ and applying the implicit Euler method to equation (B 1),

$$A_l^{k+1} - \delta_t^k U_l^{k+1} = A_l^k \quad \text{for } l = 2, \dots, L, \quad (\text{B } 13)$$

where $\delta_t^k := t^{k+1} - t^k$. Similarly, from equation (B 2), we have

$$\delta_t^k l(l+2)(l-1) A_l^{k+1} + [1 + \delta_t^k 2(2l+1)(l-1) Oh] U_l^{k+1} + \delta_t^k l B_l^{k+1} = U_l^k, \quad (\text{B } 14)$$

for $l = 2, \dots, L$,

from equation (B 3), we have

$$-\delta_t^k v^{k+1} + h^{k+1} = h^k, \quad (\text{B } 15)$$

and from equation (B 4), we have

$$-\delta_t^k B_1^{k+1} + v^{k+1} = v^k - \delta_t^k Bo; \quad (\text{B } 16)$$

which are subject to

$$\sum_{l=2}^L A_l^{k+1} P_l(\cos(\theta)) - \frac{h^{k+1}}{\cos(\theta)} = -1, \quad \text{for } \theta \leq \theta_c; \quad (\text{B } 17)$$

$$\cos(\theta) \left(1 + \sum_{l=2}^L A_l^{k+1} P_l(\cos(\theta)) \right) > h^{k+1}, \quad \text{for } \theta > \theta_c; \quad (\text{B } 18)$$

$$\sum_{l=0}^L B_l^{k+1} P_l(\cos(\theta)) = 0, \quad \text{for } \theta > \theta_c; \quad (\text{B } 19)$$

$$\frac{\partial}{\partial \theta} \left[\left(1 + \sum_{l=2}^L A_l^{k+1} P_l(\cos(\theta)) \right) \cos(\theta) \right]_{\theta=\theta_c} = 0. \quad (\text{B } 20)$$

B.2.1. Angular discretization

The spectral mesh is determined by the maximum order of harmonic modes L in our truncated expansion, using Legendre polynomials of degree 0 to L . The angular mesh

is naturally defined as the union of $\theta = 0$ (the south pole) and the zeros of $P_L(\cos(\theta))$, which is canonical for the Legendre polynomial basis (Boyd 2000). A schematic of this angular mesh is shown in figure 3(c).

The candidate integer q defines the number mesh points from the south pole to the boundary of the contact area, where the pressure is allowed to be non-zero. The boundary angle of the contact area is taken as the midpoint between θ_q and θ_{q+1} . This results in the discrete version of the constraints imposed by (B 17)-(B 20)

$$\sum_{l=2}^L A_l^{k+1,q} P_l(\cos(\theta_i)) - \frac{h^{k+1,q}}{\cos(\theta_i)} = -1, \quad \text{for } i \leq q; \quad (\text{B } 21)$$

$$\cos(\theta_i) \left(1 + \sum_{l=2}^L A_l^{k+1,q} P_l(\cos(\theta_i)) \right) > h^{k+1,q}, \quad \text{for } i > q; \quad (\text{B } 22)$$

$$\sum_{l=0}^L B_l^{k+1,q} P_l(\cos(\theta_i)) = 0, \quad \text{for } i > q; \quad (\text{B } 23)$$

and

$$\frac{\partial}{\partial \theta} \left[\left(1 + \sum_{l=2}^L A_l^{k+1,q} P_l(\cos(\theta)) \right) \cos(\theta) \right]_{(\theta_q + \theta_{q+1})/2} = 0. \quad (\text{B } 24)$$

Here, $A_l^{k+1,q}$ and $B_l^{k+1,q}$ are the amplitudes of the surface deformation and pressure distribution, respectively, obtained by solving the discrete forms of equations (B 21), (B 23), (B 25)-(B 28), assuming exactly q mesh points in the contact area:

$$A_l^{k+1,q} - \delta_t^k U_l^{k+1,q} = A_l^k, \quad \text{for } l = 2, \dots, L, \quad (\text{B } 25)$$

$$\delta_t^k l(l+2)(l-1) A_l^{k+1,q} + [1 + \delta_t^k 2(2l+1)(l-1) Oh] U_l^{k+1,q} + \delta_t^k l B_l^{k+1,q} = U_l^k, \quad \text{for } l = 2, \dots, L, \quad (\text{B } 26)$$

$$-\delta_t^k v^{k+1,q} + h^{k+1,q} = h^k, \quad (\text{B } 27)$$

and

$$-\delta_t^k B_1^{k+1,q} + v^{k+1,q} = v^k - \delta_t^k Bo, \quad (\text{B } 28)$$

where q in the superscript denotes solutions calculated assuming q contact points.

B.3. A discrete optimization problem

For a given number of contact mesh points q , we can form a closed, linear system of equations with (B 23), (B 21) and (B 25)-(B 28). We use equation (B 22) to define

$$e_q^1 = \begin{cases} 0, & \cos(\theta_i) \left(1 + \sum_{l=2}^L A_l^{k+1,q} P_l(\cos(\theta_i)) \right) > h^{k+1,q}, \text{ for all } i > q; \\ \infty, & \text{otherwise.} \end{cases} \quad (\text{B } 29)$$

This discrete version of condition (B 22) ensures the drop does not touch or penetrate the substrate outside the contact area.

For each q , the values of $A_l^{k+1,q}$ are substituted into the second-order approximation

of equation (B 24), and the absolute value of the resulting residual is computed as

$$e_q^2 = \left| \left[1 + \sum_{l=2}^L A_l^{k+1,q} P_l(\cos(\theta_q)) \right] \cos(\theta_q) - \left[1 + \sum_{l=2}^L A_l^{k+1,q} P_l(\cos(\theta_{q+1})) \right] \cos(\theta_{q+1}) \right|. \quad (\text{B } 30)$$

Finally, we define

$$e_q = \max \{e_q^1, e_q^2\}. \quad (\text{B } 31)$$

The value of q that minimises e_q defines the contact mesh points at time $k+1$; that is,

$$m^{k+1} := \operatorname{argmin}_q e_q, \quad (\text{B } 32)$$

and, consequently,

$$A_l^{k+1} := A_l^{k+1, m^{k+1}}, \quad h^{k+1} := h^{k+1, m^{k+1}}, \quad v^{k+1} := v^{k+1, m^{k+1}}, \quad (\text{B } 33)$$

$$B_l^{k+1} := B_l^{k+1, m^{k+1}}, \quad \text{and} \quad U_l^{k+1} := U_l^{k+1, m^{k+1}}. \quad (\text{B } 34)$$

B.4. The system matrices

The discretized problem involves solving a linear system of equations at each sampling time for each candidate contact area radius, parameterized by q . These systems can be expressed in matrix form as:

$$M^{k+1,q} x^{k+1,q} = b^{k+1,q}, \quad (\text{B } 35)$$

where

$$x^{k+1,q} = \left[A_2^{k+1,q}, \dots, A_L^{k+1,q}, U_2^{k+1,q}, \dots, U_L^{k+1,q}, B_0^{k+1,q}, \dots, B_L^{k+1,q}, h^{k+1,q}, v^{k+1,q} \right]^T, \quad (\text{B } 36)$$

$$b^{k+1,q} = \left[A_2^k, \dots, A_L^k, U_2^k, \dots, U_L^k, \underbrace{-1, \dots, -1}_q, \underbrace{0, \dots, 0}_{L+1-q}, h^k, v^k - \delta_t^k B_0 \right]^T, \quad (\text{B } 37)$$

and

$$\mathbf{M}^{k+1,q} = \begin{bmatrix} I_{L-1} & -\delta_t^k I_{L-1} & 0 & 0 & 0 \\ \delta_t^k C & D & \delta_t^k E & 0 & 0 \\ F^q & 0 & 0 & G^q & 0 \\ 0 & 0 & H^q & 0 & 0 \\ 0 & 0 & 0 & 1 & -\delta_t^k \\ 0 & 0 & \delta_t^k K & 0 & 1 \end{bmatrix}. \quad (\text{B } 38)$$

Here, I_m is the identity matrix of size m , and from equation (B 26) we have

$$C_{i,j} = j(j+1)(j+3) \delta_{i,j}, \quad (\text{B } 39)$$

$$D_{i,j} = (1 + \delta_t^k 2 Oh j(2j+3)) \delta_{i,j}. \quad (\text{B } 40)$$

For all $i, j = 1, 2, \dots, L-1$, where $\delta_{i,j}$ is the Kronecker delta. Also,

$$E = \left[\begin{array}{cc|ccc} 0 & 0 & 2 & 0 & \dots & \dots & 0 \\ 0 & 0 & 0 & 3 & 0 & \dots & 0 \\ \vdots & \vdots & \vdots & 0 & \ddots & & \vdots \\ \vdots & \vdots & \vdots & \vdots & & (L-1) & 0 \\ 0 & 0 & 0 & 0 & 0 & \dots & L \end{array} \right], \quad (\text{B } 41)$$

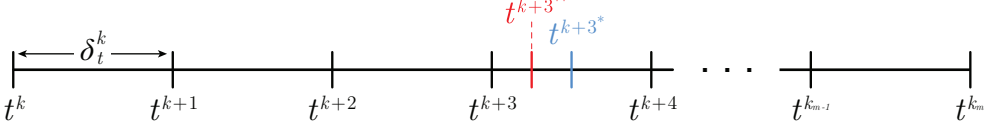


Figure 10: Time line of regularly spaced intervals (black) of spacing δ_t^k . Blue and red lines represent the time after one and two refinement steps between t^{k+3} and t^{k+4} , respectively, where δ_t^k is halved at each.

where the first two zero columns represent modes 0 and 1, absent in equation (B 26).

Similarly, from equation (B 21),

$$F_{i,j}^q = P_{j+1}(\cos(\theta_{i-1})), \quad \text{for } i = 1, 2, \dots, q; \text{ and } j = 1, 2, \dots, L-1; \quad (\text{B } 42)$$

and

$$G_i^q = \left[\frac{-1}{\cos(\theta_i)} \right], \quad \text{for } i = 1, 2, \dots, q. \quad (\text{B } 43)$$

From equation (B 23) we have

$$H_{i,j}^q = P_{j-1}(\cos(\theta_{i+q-1})), \quad \text{for } i = 1, 2, \dots, L-q+1; \text{ and } j = 1, 2, \dots, L+1; \quad (\text{B } 44)$$

and from (B 28) we obtain

$$K = \left[\underbrace{\begin{matrix} 0 & -1 & 0 & \dots & 0 \end{matrix}}_{L+1 \text{ elements}} \right]. \quad (\text{B } 45)$$

In summary, the discrete problem is reduced to finding the q that satisfies equation (B 32). Instead of solving system (B 35) for every q , we solve it for $q = m^k - 2, m^k - 1, m^k, m^k + 1, m^k + 2, \dots$. This approach significantly reduces computational costs without decreasing accuracy, enabling typical runs to complete within minutes.

Appendix C. Computational implementation

C.1. The adaptive time step

We set a maximum dimensionless step size of $2\pi / (S_L (L(L+2)(L+1))^{1/2})$, where $S_L = 16$, chosen as a fraction $1/S_L$ of the oscillation period of the fastest harmonic mode. The adaptive time step refines the initial time mesh by adding discrete times as needed. The step size is dynamically adjusted to ensure the contact area evolution is resolved with the highest accuracy permitted by the angular mesh. Specifically, if the model predicts that the number of contact mesh points m^k changes by more than one in a single step, the step is rejected, halved, and candidate solutions are recalculated. This approach relies on the assumption that the contact area evolves continuously during impact.

The code iteratively refines the time step as needed to ensure the motion of the contact area's boundary is resolved to the accuracy of the angular mesh. Figure 10 illustrates two consecutive time step refinements between t^{k+3} and t^{k+4} , following the rejection of the initial calculation t^{k+4} . This results in the insertion of t^{k+3*} , which, if also rejected, leads to the insertion of t^{k+3**} . While not shown in the figure, the discrete time sequence is renumbered to include these refinements.

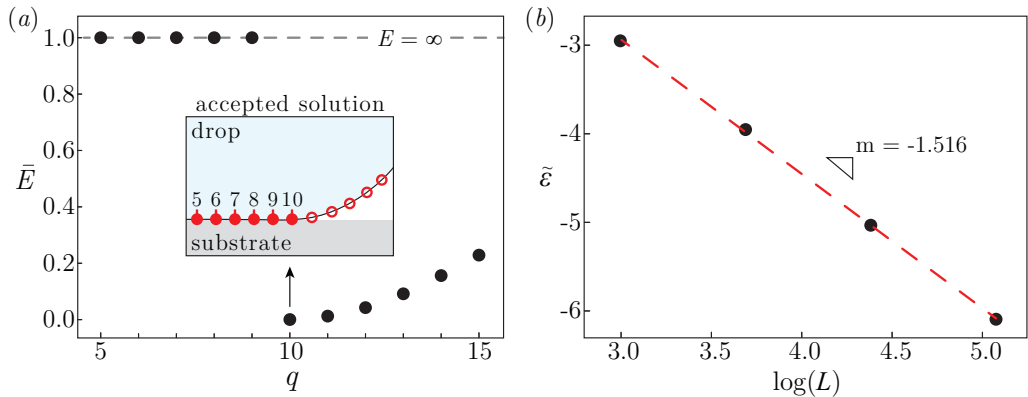


Figure 11: Normalized error $\bar{E} = 2 \tan^{-1}(E)/\pi$ versus candidate contact point q for a drop with 10 contact points. An infinite error $E = \infty$ (dashed line) is assigned for $q < 10$ using equation (B 29). For $q \geq 10$, the error is calculated using (B 30) and increases with q , showing a minimum at $q = 10$. The inset shows a schematic of the accepted solution. (b) Relative change in the coefficient of restitution $\tilde{\varepsilon} = \log(|\varepsilon_L - \varepsilon_{L/2}|/\varepsilon_{L/2})$ against number of modes $\log(L)$. The dashed line is a power law fit to the data with slope $m = -1.516$.

C.2. Finding local minima of the error

Assuming the contact area boundary moves continuously, we can reduce the computational cost of solving the discrete optimization problem in equation (B 32), which would otherwise require evaluating all possible q from 0 to L . The error in the angle between the drop and substrate (the quantity to minimize) exhibits clear monotonic behavior around the minimum. Figure 11(a) shows the normalized error $\bar{E} = 2 \tan^{-1}(E)/\pi$ plotted against q for a case where the solution indicates that $q = 10$ contact points is the optimal solution, i.e., $m^{k+1} = 10$. Our normalization of the error allows us to display both finite and infinite errors in the same plot, with $\bar{E} = 1$ for $E = \infty$.

These results indicate that to determine m^{k+1} , the number of contact points at time t^{k+1} , it is sufficient to test a subset of five values: $q = m^k - 2$ to $q = m^k + 2$. We accept only a minimum of e_q within one mesh point of m^k , and these five points provide enough information to identify any local minimum among the three acceptable points. If the minimum occurs at $q = m^k - 2$ or $q = m^k + 2$, the solution is rejected, and the time step is halved; otherwise, the solution is accepted.

In practice, we first check if $q = m^k - 1$ is a local minimum (unless $m^k = 0$). To do this, we compute the errors for $q = m^k - 2$ to $q = m^k$. If $q = m^k - 1$ is the minimum, we accept it as the correct solution. If $q = m^k - 2$ has the least error, the solution is rejected and the time step is refined. Otherwise, if $q = m^k$ has the least error, we check $q = m^k + 1$. If $q = m^k$ is confirmed as a local minimum, the solution is accepted. If not, we compute the error for $q = m^k + 2$ and either accept $q = m^k + 1$ as the solution (if it is a local minimum) or reject it and refine the time step before recalculating.

We verify whether any q causes the drop interface to intersect the substrate outside the region where pressure is allowed to be nonzero. This check is performed for all points in the angular mesh with $\theta_q < \theta_i < \pi/2$. If an intersection occurs, the error in the discrete optimization is set to ∞ . To confirm convergence in our results, we plot the relative change in the coefficient of restitution $\tilde{\varepsilon} = \log(|\varepsilon_L - \varepsilon_{L/2}|/\varepsilon_{L/2})$ for a typical rebound against number of modes $\log(L)$. A power law trend with slope $m = -1.516$ describes

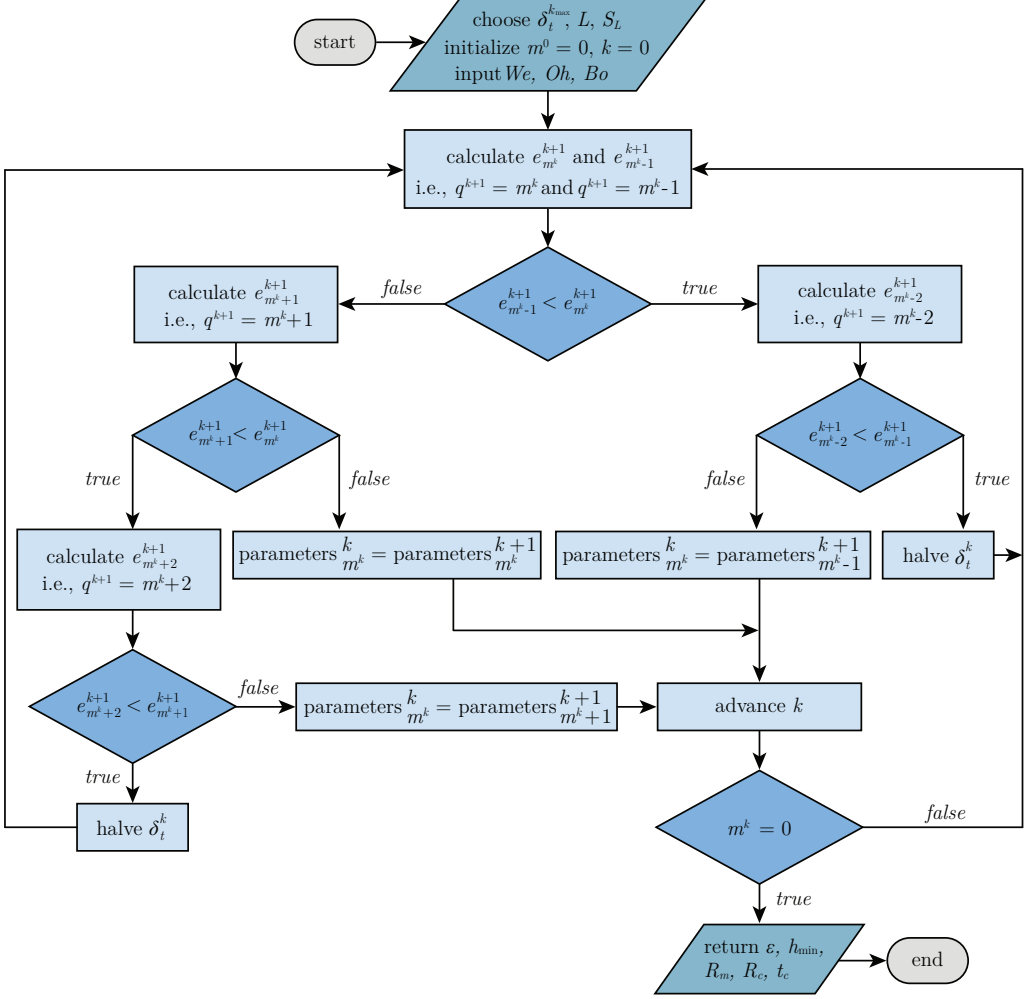


Figure 12: Flowchart of computational implementation. The return variables are the coefficient of restitution ε , minimum height of the center of mass h_{\min} , maximum equatorial radius R_m , maximum spreading radius R_c and contact time t_c .

the convergence our results and motivates our choice of $L = 90$ throughout this work. A flowchart for this procedure is presented in figure 12.

REFERENCES

- AGÜERO, E.A., ALVENTOSA, L., HARRIS, D.M. & GALEANO-RIOS, C.A. 2022 Impact of a rigid sphere onto an elastic membrane. *Proceedings of the Royal Society A* **478** (2266), 20220340.
- ALVENTOSA, L.F.L., CIMPEANU, R. & HARRIS, D.M. 2023 Inertio-capillary rebound of a droplet impacting a fluid bath. *Journal of Fluid Mechanics* **958**, A24.
- ANDERS, K., ROTH, N. & FROHN, A. 1993 The velocity change of ethanol droplets during collision with a wall analysed by image processing. *Experiments in Fluids* **15**, 91–96.
- AUSSILLOUS, P. & QUÉRÉ, D. 2006 Properties of liquid marbles. *Proceedings of the Royal Society A: Mathematical, Physical and Engineering Sciences* **462** (2067), 973–999.

- BACH, G.A., KOCH, D.L. & GOPINATH, A. 2004 Coalescence and bouncing of small aerosol droplets. *Journal of Fluid Mechanics* **518**, 157–185.
- BARTHLOTT, W. & NEINHUIS, C. 1997 Purity of the sacred lotus, or escape from contamination in biological surfaces. *Planta* **202** (1), 1–8.
- BARTOLO, D., BOUDAUD, A., NARCY, G. & BONN, D. 2007 Dynamics of non-newtonian droplets. *Physical Review Letters* **99** (17), 174502.
- BARTOLO, D., JOSSEAND, C. & BONN, D. 2005 Retraction dynamics of aqueous drops upon impact on non-wetting surfaces. *Journal of Fluid Mechanics* **545**, 329–338.
- BARTOLO, D., JOSSEAND, C. & BONN, D. 2006 Singular jets and bubbles in drop impact. *Physical Review Letters* **96** (12), 124501.
- BASSO, B.C. & BOSTWICK, J.B. 2020 Splashing on soft elastic substrates. *Langmuir* **36** (49), 15010–15017.
- BENNETT, T. & POULIKAKOS, D. 1993 Splat-quench solidification: estimating the maximum spreading of a droplet impacting a solid surface. *Journal of Materials Science* **28**, 963–970.
- BIANCE, A.L., CHEVY, F., CLANET, C., LAGUBEAU, G. & QUÉRÉ, D. 2006 On the elasticity of an inertial liquid shock. *Journal of Fluid Mechanics* **554**, 47–66.
- BOUROUBA, LYDIA 2021 The fluid dynamics of disease transmission. *Annual Review of Fluid Mechanics* **53** (1), 473–508.
- BOYD, J. 2000 *Chebyshev and Fourier Spectral Methods*. DOVER Publications, Inc.
- CHANDRA, S. & AVEDISIAN, C.T. 1991 On the collision of a droplet with a solid surface. *Proceedings of the Royal Society of London. Series A: Mathematical and Physical Sciences* **432** (1884), 13–41.
- CHEN, L., XIAO, Z., CHAN, P.C.H., LEE, Y.K. & LI, Z. 2011 A comparative study of droplet impact dynamics on a dual-scaled superhydrophobic surface and lotus leaf. *Applied Surface Science* **257** (21), 8857–8863.
- CHEN, S. & ASHGRIZ, N. 2022 Droplet size distribution in swirl nozzles. *International Journal of Multiphase Flow* **156**, 104219.
- CHEVY, F., CHEPELIANSKII, A., QUÉRÉ, D. & RAPHAËL, E. 2012 Liquid hertz contact: Softness of weakly deformed drops on non-wetting substrates. *Europhysics Letters* **100** (5), 54002.
- CHUBYNSKY, M.V., BELOUSOV, K.I., LOCKERBY, D.A. & SPRITTLES, J.E. 2020 Bouncing off the walls: the influence of gas-kinetic and van der waals effects in drop impact. *Physical Review Letters* **124** (8), 084501.
- CLANET, C., BÉGUIN, C., RICHARD, D. & QUÉRÉ, D. 2004 Maximal deformation of an impacting drop. *Journal of Fluid Mechanics* **517**, 199–208.
- COUDER, Y., FORT, E., GAUTIER, C.-H. & BOUDAUD, A. 2005a From bouncing to floating: noncoalescence of drops on a fluid bath. *Physical Review Letters* **94** (17), 177801.
- COUDER, Y., PROTIERE, S., FORT, E. & BOUDAUD, A. 2005b Walking and orbiting droplets. *Nature* **437** (7056), 208–208.
- DBOUK, T. & DRIKAKIS, D. 2020 On coughing and airborne droplet transmission to humans. *Physics of Fluids* **32** (5).
- DE RUITER, J., LAGRAAUW, R., VAN DEN ENDE, D. & MUGELE, F. 2015 Wettability-independent bouncing on flat surfaces mediated by thin air films. *Nature physics* **11** (1), 48–53.
- DÍAZ, DIEGO, GARCIA-GONZALEZ, DIANA, BISTA, PRAVASH, WEBER, STEFAN AL, BUTT, HANS-JÜRGEN, STETTEN, AMY & KAPPL, MICHAEL 2022 Charging of drops impacting onto superhydrophobic surfaces. *Soft Matter* **18** (8), 1628–1635.
- EDGERTON, H.E. & KILLIAN, J.R. 1954 Flash!: Seeing the unseen by ultra high-speed photography pp. 116–123.
- EGGERS, J., FONTELOS, M.A., JOSSEAND, C. & ZALESKI, S. 2010 Drop dynamics after impact on a solid wall: theory and simulations. *Physics of Fluids* **22** (6).
- FALDE, E.J., YOHE, S.T., COLSON, Y.L. & GRINSTAFF, MARK W. 2016 Superhydrophobic materials for biomedical applications. *Biomaterials* **104**, 87–103.
- FOOTE, G.B. 1975 The water drop rebound problem: dynamics of collision. *Journal of Atmospheric Sciences* **32** (2), 390–402.
- GALEANO-RIOS, C.A., CIMPEANU, R., BAUMAN, I.A., MAC EWEN, A., MILEWSKI, P.A.

- & HARRIS, D.M. 2021 Capillary-scale solid rebounds: experiments, modelling and simulations. *Journal of Fluid Mechanics* **912**, A17.
- GALEANO-RIOS, C.A., MILEWSKI, P.A. & VANDEN-BROECK, J.-M. 2017 Non-wetting impact of a sphere onto a bath and its application to bouncing droplets. *Journal of Fluid Mechanics* **826**, 97–127.
- GALEANO-RIOS, C.A., MILEWSKI, P.A. & VANDEN-BROECK, J.-M. 2019 Quasi-normal free-surface impacts, capillary rebounds and application to faraday walkers. *Journal of Fluid Mechanics* **873**, 856–888.
- GARCÍA-GEIJO, P., RIBOUX, G. & GORDILLO, J.M. 2020 Inclined impact of drops. *Journal of Fluid Mechanics* **897**, A12.
- GILET, T. & BUSH, J.W.M. 2012 Droplets bouncing on a wet, inclined surface. *Physics of Fluids* **24** (12).
- GILET, T., TERWAGNE, D., VANDEWALLE, N. & DORBOLO, S. 2008 Dynamics of a bouncing droplet onto a vertically vibrated interface. *Physical Review Letters* **100** (16), 167802.
- HAO, C., LI, J., LIU, Y., ZHOU, X., LIU, Y., LIU, R., CHE, L., ZHOU, W., SUN, D., LI, L., XU, L. & WANG, Z. 2015 Superhydrophobic-like tunable droplet bouncing on slippery liquid interfaces. *Nature Communications* **6** (1), 7986.
- HARRIS, D.M., LIU, T. & BUSH, J.W.M. 2015 A low-cost, precise piezoelectric droplet-on-demand generator. *Experiments in Fluids* **56**, 1–7.
- HIRT, C.W. & NICHOLS, B.D. 1981 Volume of fluid (vof) method for the dynamics of free boundaries. *Journal of Computational Physics* **39** (1), 201–225.
- IONKIN, N. & HARRIS, D.M. 2018 Note: A versatile 3d-printed droplet-on-demand generator. *Review of Scientific Instruments* **89** (11).
- JHA, A., CHANTELOT, P., CLANET, C. & QUÉRÉ, D. 2020 Viscous bouncing. *Soft Matter* **16** (31), 7270–7273.
- JOSSERAND, C. & THORODDSSEN, S.T. 2016 Drop impact on a solid surface. *Annual Review of Fluid Mechanics* **48** (1), 365–391.
- KAVEHPOUR, H.P. 2015 Coalescence of drops. *Annual Review of Fluid Mechanics* **47** (1), 245–268.
- KOLINSKI, JOHN M, RUBINSTEIN, SHMUEL M, MANDRE, SHREYAS, BRENNER, MICHAEL P, WEITZ, DAVID A & MAHADEVAN, L 2012 Skating on a film of air: drops impacting on a surface. *Physical review letters* **108** (7), 074503.
- KOOIJ, S., SIJS, R., DENN, M.M., VILLERMAUX, E. & BONN, D. 2018 What determines the drop size in sprays? *Physical Review X* **8** (3), 031019.
- LAAN, N., DE BRUIN, K.G., BARTOLO, D., JOSSERAND, C. & BONN, D. 2014 Maximum diameter of impacting liquid droplets. *Physical Review Applied* **2** (4), 044018.
- LAMB, HORACE 1924 *Hydrodynamics*. Cambridge University Press.
- LEE, J.B., LAAN, N., DE BRUIN, K.G., SKANTZARIS, G., SHAHIDZADEH, N., DEROME, D., CARMELIET, J. & BONN, D. 2016 Universal rescaling of drop impact on smooth and rough surfaces. *Journal of Fluid Mechanics* **786**, R4.
- LEWIN-JONES, P., LOCKERBY, D.A. & SPRITTLES, J.E. 2024 Collision of liquid drops: bounce or merge? *Journal of Fluid Mechanics* **995**, A1.
- LI, Y.-J., LIU, Y.-Z., WANG, Y.-B. & CHEN, M. 2024 Rebound dynamics of inverse leidenfrost droplets on dry ice surfaces. *Physical Review Fluids* **9** (9), 093601.
- LIN, S., SHI, D., ZHOU, L., CHEN, L. & LI, Z. 2024 Probing the contact time of droplet impacts: From the hertz collision to oscillation regimes. *Physical Review E* **110** (5), L053101.
- LIU, Y., LIU, Y. & CHEN, M. 2023 Maximum spreading diameter of bouncing droplets at ultralow weber numbers. *Langmuir* **39** (22), 7922–7929.
- LO, H.Y., LIU, Y. & XU, L. 2017 Mechanism of contact between a droplet and an atomically smooth substrate. *Physical Review X* **7** (2), 021036.
- LOHSE, D. 2022 Fundamental fluid dynamics challenges in inkjet printing. *Annual Review of Fluid Mechanics* **54** (1), 349–382.
- MAKHNENKO, I., ALONZI, E.R., FREDERICKS, S.A., COLBY, C.M. & DUTCHER, C.S. 2021 A review of liquid sheet breakup: Perspectives from agricultural sprays. *Journal of Aerosol Science* **157**, 105805.
- MILLER, CA & SCRIVEN, LE 1968 The oscillations of a fluid droplet immersed in another fluid. *Journal of Fluid Mechanics* **32** (3), 417–435.

- MOLÁČEK, J. & BUSH, J.W.M. 2012 A quasi-static model of drop impact. *Physics of Fluids* **24** (12).
- MOLÁČEK, JAN & BUSH, JOHN WM 2013 Drops walking on a vibrating bath: towards a hydrodynamic pilot-wave theory. *Journal of Fluid Mechanics* **727**, 612–647.
- OKUMURA, K., CHEVY, F., RICHARD, D., QUÉRÉ, D. & CLANET, C. 2003 Water spring: A model for bouncing drops. *Europhysics Letters* **62** (2), 237.
- PHILLIPS, K.A. & MILEWSKI, P.A. 2024 Lubrication-mediated rebounds off fluid baths. *Journal of Fluid Mechanics* **1000**, R2.
- POPINET, S. 2009 An accurate adaptive solver for surface-tension-driven interfacial flows. *Journal of Computational Physics* **228** (16), 5838–5866.
- POPINET, S. 2015 A quadtree-adaptive multigrid solver for the Serre–Green–Naghdi equations. *Journal of Computational Physics* **302**, 336–358.
- RAYLEIGH, LORD 1879 On the capillary phenomena of jets. *Proceedings of the Royal Society of London* pp. 71–97.
- RAYLEIGH, LORD 1899 Xxxvi. investigations in capillarity:—the size of drops.—the liberation of gas from supersaturated solutions.—colliding jets.—the tension of contaminated water-surfaces. *The London, Edinburgh, and Dublin Philosophical Magazine and Journal of Science* **48** (293), 321–337.
- REIN, M. 1993 Phenomena of liquid drop impact on solid and liquid surfaces. *Fluid Dynamics Research* **12** (2), 61–93.
- RICHARD, D., CLANET, C. & QUÉRÉ, D. 2002 Contact time of a bouncing drop. *Nature* **417** (6891), 811–811.
- RICHARD, D. & QUÉRÉ, D. 2000 Bouncing water drops. *Europhysics Letters* **50** (6), 769.
- ROISMAN, I.V. 2009 Inertia dominated drop collisions. ii. an analytical solution of the navier–stokes equations for a spreading viscous film. *Physics of Fluids* **21** (5).
- ROTH-NEBELSICK, A., KONRAD, W., EBNER, M., MIRANDA, T., THIELEN, S. & NEBELSICK, J.H. 2022 When rain collides with plants—patterns and forces of drop impact and how leaves respond to them. *Journal of Experimental Botany* **73** (4), 1155–1175.
- DE RUITER, J., OH, J.M., VAN DEN ENDE, D. & MUGELE, F. 2012 Dynamics of collapse of air films in drop impact. *Physical Review Letters* **108** (7), 074505.
- SANJAY, V., CHANTELOT, P. & LOHSE, D. 2023a When does an impacting drop stop bouncing? *Journal of Fluid Mechanics* **958**, A26.
- SANJAY, V., LAKSHMAN, S., CHANTELOT, P., SNOEIJER, J.H. & LOHSE, D. 2023b Drop impact on viscous liquid films. *Journal of Fluid Mechanics* **958**, A25.
- SANJAY, VATSAL & LOHSE, DETLEF 2025 Unifying theory of scaling in drop impact: Forces and maximum spreading diameter. *Physical Review Letters* **134**, 104003.
- SAYLOR, J.R. & BOUNDS, G.D. 2012 Experimental study of the role of the weber and capillary numbers on mesler entrainment. *AIChE Journal* **58** (12), 3841–3851.
- SCARDOVELLI, R. & ZALESKI, S. 1999 Direct numerical simulation of free-surface and interfacial flow. *Annual Review of Fluid Mechanics* **31** (1), 567–603.
- SHIRI, S. & BIRD, J.C. 2017 Heat exchange between a bouncing drop and a superhydrophobic substrate. *Proceedings of the National Academy of Sciences* **114** (27), 6930–6935.
- SPRITTLES, J.E. 2024 Gas microfilms in droplet dynamics: When do drops bounce? *Annual Review of Fluid Mechanics* **56** (1), 91–118.
- THENARIANTO, C., KOH, X.Q., LIN, M., JOKINEN, V. & DANIEL, D. 2023 Energy loss for droplets bouncing off superhydrophobic surfaces. *Langmuir* **39** (8), 3162–3167.
- TSAI, P., HENDRIX, M.H.W., DIJKSTRA, R.R.M., SHUI, L. & LOHSE, D. 2011 Microscopic structure influencing macroscopic splash at high weber number. *Soft Matter* **7** (24), 11325–11333.
- VILLERMAUX, E. 2020 Fragmentation versus cohesion. *Journal of Fluid Mechanics* **898**, P1.
- VILLERMAUX, E. & BOSSA, B. 2011 Drop fragmentation on impact. *Journal of Fluid Mechanics* **668**, 412–435.
- WANG, Y., ZHAO, Y., SUN, L., MEHRIZI, A.A., LIN, S., GUO, J. & CHEN, L. 2022 Successive rebounds of impinging water droplets on superhydrophobic surfaces. *Langmuir* **38** (12), 3860–3867.
- WILLIS, K.D. & ORME, M.E. 2000 Experiments on the dynamics of droplet collisions in a vacuum. *Experiments in Fluids* **29** (4), 347–358.

- WORTHINGTON, A.M. 1877 Xxviii. on the forms assumed by drops of liquids falling vertically on a horizontal plate. *Proceedings of the Royal Society of London* **25** (171-178), 261–272.
- WORTHINGTON, A.M. 1908 *A study of splashes*. Longmans, Green, and Company.
- WU, ZHIHU, HAO, JIGUANG, LU, JIE, XU, LONG, HU, GENGKAI & FLORYAN, JM 2020 Small droplet bouncing on a deep pool. *Physics of Fluids* **32** (1).
- YARIN, A.L. 2006 Drop impact dynamics: splashing, spreading, receding, bouncing. . . . *Annual Review of Fluid Mechanics* **38** (1), 159–192.
- YUN, S. & KIM, I. 2019 Spreading dynamics and the residence time of ellipsoidal drops on a solid surface. *Langmuir* **35** (40), 13062–13069.
- ZHAN, H., LU, C., LIU, C., WANG, Z., LV, C. & LIU, Y. 2021 Horizontal motion of a superhydrophobic substrate affects the drop bouncing dynamics. *Physical Review Letters* **126** (23), 234503.
- ZHAO, HE, BRUNSVOLD, AMY & MUNKEJORD, SVEND TOLLAK 2011 Transition between coalescence and bouncing of droplets on a deep liquid pool. *International Journal of Multiphase Flow* **37** (9), 1109–1119.